Chinese Journal of Aeronautics, (2024), 37(10): 136–157



Chinese Society of Aeronautics and Astronautics
& Beihang University

Chinese Journal of Aeronautics

cja@buaa.edu.cn
www.sciencedirect.com



FULL LENGTH ARTICLE

Numerical study on ignition start-up process of an underwater solid rocket motor across a wide depth range



Deyou WANG [a], **Shipeng LI** [a,*], **Ge JIN** [a], **Ruyao WANG** [a], **Dian GUAN** [b], **Ningfei WANG** [a]

[a] *School of Aerospace Engineering, Beijing Institute of Technology, Beijing 100081, China*
[b] *Beijing System Design Institute of Electro-mechanic Engineering, Beijing 100854, China*

Received 6 November 2023; revised 28 November 2023; accepted 19 January 2024
Available online 24 June 2024

KEYWORDS

Underwater propulsion;
Solid rocket motor;
Ignition start-up process;
Underwater gas jet;
Thrust oscillation

Abstract Solid rocket motors have important applications in the propulsion of trans-media vehicles and underwater launched rockets. In this paper, the ignition start-up process of an underwater solid rocket motor across a wide depth range has been numerically studied. A novel multi-domain integrated model has been developed by combining the solid propellant ignition and combustion model with the volume of fluid multiphase model. This integrated model enables the coupled simulation of the propellant combustion and gas flow inside the motor, along with the gas jet evolution in the external water environment. The detailed flow field developments in the combustion chamber, nozzle, and wake field are carefully analyzed. The variation rules of the internal ballistics and thrust performance are also obtained. The effects of environmental medium and operating depth on the ignition start-up process are systematically discussed. The results show that the influence of the operating environment on the internal ballistic characteristics is primarily reflected in the initial period after the nozzle closure opens. The development of the gas jet in water lags significantly compared with that in air. As the water depth increases, the ignition delay time of the motor is shortened, and the morphology evolution of the gas jet is significantly compressed and accelerated. Furthermore, the necking and bulging of the jet boundary near the nozzle outlet and the consequent shock oscillations are intensified, resulting in stronger fluctuations in the wake pressure field and motor thrust.

© 2024 Production and hosting by Elsevier Ltd. on behalf of Chinese Society of Aeronautics and Astronautics. This is an open access article under the CC BY-NC-ND license (http://creativecommons.org/licenses/by-nc-nd/4.0/).

* Corresponding author.
E-mail address: lsp@bit.edu.cn (S. LI).
Please check the inserted running head and correct if necessary.



1. Introduction

Solid Rocket Motors (SRMs) are widely used as propulsion systems for rockets and missiles. The application of SRMs in underwater propulsion is getting more and more concern

https://doi.org/10.1016/j.cja.2024.06.019
1000-9361 © 2024 Production and hosting by Elsevier Ltd. on behalf of Chinese Society of Aeronautics and Astronautics.
This is an open access article under the CC BY-NC-ND license (http://creativecommons.org/licenses/by-nc-nd/4.0/).

Nomenclature

a	Burning rate coefficient
A	Area
c	Specific heat
C_F	Thrust coefficient
E	Energy
F	Thrust
g	Gravitational acceleration
h	Convective heat transfer coefficient
H	Water depth
$\boldsymbol{I}$	Unit tensor
k	Turbulence kinetic energy
M	Molecular weight
Ma	Mach number
n	Burning rate pressure exponent
p	Pressure
$\dot{r}$	Propellant burning rate
R	Radius
Δt	Ignition delay time
Δt_1	Ignition induction period
Δt_2	Flame-spreading period
Δt_3	Chamber-filling period
R_g	Gas constant of propellant gas
$\boldsymbol{S}_f$	Momentum source term
S_h	Energy source term
S_m	Mass source term
t	Time
T	Temperature
T_c	Critical ignition temperature
$\boldsymbol{u}$	Velocity vector
V_c	Added-mass cell volume

Greek symbols

α	Phase volume fraction
γ	Specific heat ratio of propellant gas
ε	Turbulence dissipation rate
λ	Thermal conductivity
μ	Viscosity
ρ	Density
$\boldsymbol{\tau}$	Stress tensor

Subscripts

0	Basic
a	Ambient
atm	Atmospheric
b	Burning surface or back wall
c	Combustion chamber
e	Erosion or nozzle exit
eff	Effective
eq	Equilibrium
ext	External
g	Propellant gas or gas phase
ig	Ignition gas
intl	Internal
o	Opening of nozzle closure
p	Propellant
t	Turbulence or nozzle throat
w	Water or propellant surface

and attention, providing more possibilities for the propulsion of trans-media vehicles and underwater launched rockets. Although there have been some new techniques with potentiality, such as water ramjet engines,[1,2] SRMs are still the better choice for military applications such as submarine-launched missiles and rising mines due to their outstanding advantages of fast response, high reliability, long-term standby, and low cost. When the SRM is operating, the high-temperature and high-pressure gas produced by solid propellant combustion is exhausted at high speed after the energy conversion of the nozzle, and then the forward thrust is generated. However, in a water environment, the expansion flow of the gas is severely blocked by the high-density water medium (about 800 times the density of air). Especially when in deep water, the high ambient pressure causes the gas phase to be compressed to a greater extent, resulting in a highly over-expanded state of the nozzle with unwanted flow separation.[3–5] Due to the complex interaction between high-speed gas flow and water, the nozzle exhaust jet usually exhibits a strong unsteadiness, which makes the thrust performance of the SRM challenging to predict.

The ignition start-up process of an underwater SRM is very complex. From the perspective of time sequence, events include igniter gas injection, propellant heating and ignition, flame spreading, chamber pressurization, nozzle closure opening, gas bubble formation, and supersonic gas jet evolution. From the space perspective, it involves multi-field multiphase transient flows in the combustion chamber, nozzle, and external water environment. The ignition start-up process is highly essential for the reliable operation of SRMs. Abnormalities in this process may lead to flameout, intermittent combustion, structural failure, or even disastrous consequences, such as explosion. Considering the high cost of experimental testing and the limited measurement data, numerical simulation has become an important method for studying the ignition transient of SRMs. There have been many studies using one-dimensional, two-dimensional, or three-dimensional models to describe the flow field characteristics in ignition transients.[6–11] Furthermore, more complex codes for multidimensional fluid–structure coupled simulation have been developed to consider the mechanical response of solid propellants.[12–16] Previous studies on the ignition transient of SRMs focus mainly on the propellant ignition, fluid flow, and structural response inside the combustion chamber. However, the ignition start-up process of SRMs in a water environment has not been fully studied yet in the open literature.

A highly turbulent, strongly transient momentum jet will be formed as the high-pressure combustion gas is injected into water at supersonic speed from the nozzle. Such phenomena of underwater supersonic gaseous jets have been studied extensively over the past few decades. Loth and Faeth[17,18] conducted experiments on the structures of round and planar

under-expanded air jets in a water-filled tank. The flow visualization indicated the presence of shock-wave-containing external-expansion regions, which decayed more rapidly than air-to-air jets due to the intense gas–liquid mixing. Dai et al.[19] experimentally studied the upstream pressure oscillations induced by supersonic gas jets in still water. The measurements showed that the upstream sidewall pressures were characterized by large discrete pulsations superposed on small continuous fluctuations. Shi et al.[20,21] conducted a series of experimental studies on the oscillation flow characteristics of underwater supersonic gas jets exhausted from Laval nozzles in a water tank. They reported the bulging and back-attack behaviors of the jet during its development, and they proposed that the back-attack was essentially a kind of shock wave feedback phenomenon through pressure measurements. Weiland and Vlachos[22] evaluated the pinch-off location, penetration distance, and unsteady interface characteristics of underwater round supersonic gas jets through similar experiments. Due to the velocity shear and density differences between the gas–liquid phases, as well as the shock/jet interface interactions,[23,24] the supersonic gas jets submerged in water are highly unstable. Zhang et al.[25,26] conducted experiments of supersonic gaseous jets under different water depths in a pressurized water vessel. They found that such instability at the jet interface would be intensified as the water depth increases. Considering the difficulties inherent to the visualization and experimental measurement of jet interiors, there have been many studies using numerical methods to analyze the flow structures of underwater supersonic gas jets. Tang et al.[27] analyzed the typical phenomena such as expansion, bulging, necking/breaking, and back-attack in the jet process using computational simulation. They pointed out that the oscillatory thrust of the underwater propulsion system was caused by the intermittent pulses of back pressure and nozzle exit pressure. Zhang et al.[28] simulated the flow field of supersonic gaseous jets in deep water. The results revealed that the flow oscillations were related to the turbulent gas–water mixing and the unstable motion of shock waves along the central gas path. Similar numerical studies were also addressed by Fronzeo,[29] Tang,[30,31] Gong,[32] Liu,[33] and Jana[34] et al. In their research, the effects of ambient fluid density, buoyant effect, water depth, and operating pressure ratio on the jet flow characteristics and nozzle thrust performance were evaluated in detail. In general, water depth, nozzle expansion ratio, and inlet total pressure are the main factors affecting bubble formation and development for underwater supersonic gas jets.

The previous studies listed above focus mainly on the underwater supersonic gas jet itself, lacking consideration from the propulsion system level. For now, there have been several experimental evaluations of the underwater operating characteristics for propulsion systems such as solid rocket motors,[35,36] hybrid rocket motors,[37] and pulse detonation engines.[38,39] Nevertheless, to the best of our knowledge, there are almost no numerical studies on the detailed process of underwater ignition start-up for SRMs, especially for the overall performance at a great water depth. On the other hand, in almost all previous numerical studies, the nozzle inlet has been treated as a simple pressure inlet with a constant pressure value or a prescribed pressure profile. This simplification decouples the development of the external underwater gas jet from the propellant combustion and gas generation inside the combustion chamber. Due to the large gap with the practical situation of underwater propulsion, such simplified models have significant limitations in studying the operating characteristics of underwater SRMs, especially for the transient flow during the early stage of ignition. In practical application, the SRMs may face the ignition and operation at different depths. Therefore, the current study is motivated by the need for a comprehensive understanding of the flow mechanisms and performance characteristics during the ignition start-up process of SRMs across a wide depth range from the perspective of real physical processes.

This paper aims at developing a multi-domain integrated model to simulate the ignition start-up process of an underwater SRM across a wide depth range. The combination of the solid propellant ignition and combustion model with the Volume of Fluid (VOF) multiphase model is employed. Through numerical simulation, the flow characteristics in the combustion chamber, nozzle, and wake field are analyzed, the variation rules of the internal ballistics and thrust performance are obtained, and the effects of environmental medium and operating depth are discussed. The remainder of this paper is organized as follows. Section 2 introduces the governing equations and numerical models involved in the simulation. Section 3 reports the validation of the numerical method. Section 4 introduces the physical and computational models. Section 5 analyzes numerical results of the underwater ignition start-up process for an SRM across a wide depth range.

2. Numerical simulation method

2.1. Governing equations

To simulate the underwater ignition start-up process of an SRM, the gas flow in the combustion chamber and the supersonic gas jet evolution in the water environment must be fully considered. This typical unsteady, compressible, multiphase flow process involves many complex problems, such as propellant ignition and combustion modeling, supersonic flow calculation, gas–liquid interface tracking, and turbulent mixing simulation. In the present study, the propellant gas is approximated as a compressible ideal gas, and the liquid water is treated as an incompressible fluid. Based on the understanding of the above problems, the basic governing equations are described as follows.[40]

Mass conservation equation:

$$\frac{\partial \rho}{\partial t} + \nabla \cdot (\rho \boldsymbol{u}) = S_{\mathrm{m}} \tag{1}$$

where ρ is the density of the mixture, and it can be defined as $\rho = \alpha_1\rho_1 + \alpha_2\rho_2$. Among that, ρ_1 and ρ_2 are the densities of gas and water, respectively. α_1 and α_2 are the phase volume fractions of gas and water, respectively. $\boldsymbol{u}$ is the velocity vector, and S_{m} is the mass source term.

Momentum conservation equation:

$$\frac{\partial}{\partial t}(\rho \boldsymbol{u}) + \nabla \cdot (\rho \boldsymbol{u}\boldsymbol{u}) = -\nabla p + \nabla \cdot \boldsymbol{\tau} + \boldsymbol{S}_{\mathrm{f}} \tag{2}$$

where p is the fluid pressure in the flow field, $\boldsymbol{\tau}$ is the stress tensor, and $\boldsymbol{S}_{\mathrm{f}}$ is the momentum source term. The expression of $\boldsymbol{\tau}$ can be written as follows:

$$\boldsymbol{\tau} = \mu\left[\left(\nabla \boldsymbol{u} + \nabla \boldsymbol{u}^{\mathrm{T}}\right) - \frac{2}{3}(\nabla \cdot \boldsymbol{u})\boldsymbol{I}\right] \tag{3}$$

where μ is the viscosity of the mixture, and similarly it can be defined as $\mu = \alpha_1\mu_1 + \alpha_2\mu_2$. $\boldsymbol{I}$ is the unit tensor.

Energy conservation equation:

$$\frac{\partial}{\partial t}(\rho E) + \nabla \cdot [\boldsymbol{u}(\rho E + p)] = \nabla \cdot [\lambda_{\text{eff}} \nabla T + (\boldsymbol{\tau}_{\text{eff}} \cdot \boldsymbol{u})] + S_{\text{h}} \tag{4}$$

where E and T are respectively the energy and temperature of the mixture, λ_{eff} is the effective thermal conductivity, $\boldsymbol{\tau}_{\text{eff}}$ is the effective stress tensor, and S_{h} is the energy source term. Here, E and T are treated as mass-averaged variables whose values can be calculated by following relations:

$$E = \frac{\sum_{q=1}^{2} \alpha_q \rho_q E_q}{\sum_{q=1}^{2} \alpha_q \rho_q}, T = \frac{\sum_{q=1}^{2} \alpha_q \rho_q T_q}{\sum_{q=1}^{2} \alpha_q \rho_q} \tag{5}$$

Gas state equation:

$$p = \rho_{\text{g}} R_{\text{g}} T \tag{6}$$

where ρ_{g} and R_{g} are the density and gas constant of propellant gas, respectively.

2.2. VOF multiphase model

The gas–liquid interface of the jet is captured using the VOF multiphase model. This model has been widely used in the prediction of jet breakup, the motion of large bubbles in a liquid, and dam-break problems in engineering. For the simulation of high-pressure gas jet evolution in a water environment, the VOF model has been fully validated in related studies.[25–31] For phase q, the volume fraction conservation equation has the following form:

$$\frac{\partial}{\partial t}(\alpha_q \rho_q) + \nabla \cdot (\alpha_q \rho_q \boldsymbol{u}_q) = S_{\alpha_q} + \sum_{p=1}^{n} (\dot{m}_{pq} - \dot{m}_{qp}) \tag{7}$$

where α_q, ρ_q, and $\boldsymbol{u}_q$ are the volume fraction, density, and velocity of phase q, respectively, S_{α_q} is the source item of phase q, $\dot{m}_{pq}$ is the mass transfer from phase p to phase q, and $\dot{m}_{qp}$ is the mass transfer from phase q to phase p. The phase volume fractions satisfy the following constraint:

$$\sum_{q=1}^{n} \alpha_q = 1 \tag{8}$$

In this study, propellant gas is defined as the primary phase and liquid water as the secondary phase. The chemical reactions and mass transfer between the gas and liquid phases are ignored. The density of liquid water is 998.2 kg/m^3, and the dynamic viscosity is 1.003×10^{-3} Pa·s. For the liquid phase, the right-hand of the volume fraction conservation equation is zero.

2.3. Turbulence model

The standard k-ε model is adopted to describe the turbulent flow based on the practice of related studies. This two-equation semi-empirical model for high Reynolds number flows is widely used in practical engineering flow calculations, and is also applicable to multiphase flows. In Refs. 9, 41–43, this model has been used for simulating the ignition transient of an end-burning-grain SRM and the expansion process of multiple high-pressure gas jets in a water-filled vessel, respectively. The numerical results are in good agreement with the experimental measurements, indicating the validity of the model for simulating the gas flow in the combustion chamber and the gas–liquid two-phase flow of underwater supersonic gas jets. The turbulence kinetic energy k and its rate of dissipation ε are obtained from the following transport equations:

$$\frac{\partial(\rho k)}{\partial t} + \frac{\partial(\rho k u_i)}{\partial x_i} = \frac{\partial}{\partial x_j}\left[\left(\mu + \frac{\mu_{\text{t}}}{\sigma_k}\right)\frac{\partial k}{\partial x_j}\right] + G_k - \rho\varepsilon - Y_{\text{M}} \tag{9}$$

$$\frac{\partial(\rho \varepsilon)}{\partial t} + \frac{\partial(\rho \varepsilon u_i)}{\partial x_i} = \frac{\partial}{\partial x_j}\left[\left(\mu + \frac{\mu_{\text{t}}}{\sigma_\varepsilon}\right)\frac{\partial \varepsilon}{\partial x_j}\right] + C_{1\varepsilon}\frac{\varepsilon}{k}G_k - C_{2\varepsilon}\rho\frac{\varepsilon^2}{k} \tag{10}$$

where $\mu_{\text{t}} = \rho C_\mu k^2/\varepsilon$ is the turbulent viscosity. The constants $\sigma_k = 1.0$ and $\sigma_\varepsilon = 1.3$ are the turbulent Prandtl numbers for k and ε, respectively. G_k represents the generation of turbulence kinetic energy due to the mean velocity gradients. Y_M represents the contribution of the fluctuating dilatation in compressible turbulence to the overall dissipation rate. The constants $C_{1\varepsilon} = 1.44$, $C_{2\varepsilon} = 1.92$, and $C_\mu = 0.09$ are empirical coefficients.

2.4. Solid propellant ignition and combustion model

The ignition and combustion process of solid propellant involves very complex physical and chemical phenomena. It is impractical to accurately describe all these phenomena in the numerical simulation. In this study, a simplified numerical model has been developed to simulate the propellant ignition and combustion process. The widely accepted ignition temperature criterion is employed to determine whether the propellant surface is burning.[9] The conjugate heat transfer method is used to calculate the propellant surface temperature to describe the heating process of the propellant grain by the high-temperature gas. For simplicity, the solid phase chemical reactions and the radiative heat transfer before propellant ignition are ignored. The governing equation of solid phase is the heat conduction equation:

$$\frac{\partial T_{\text{p}}}{\partial t} = \frac{\lambda_{\text{p}}}{\rho_{\text{p}} c_{\text{p}}} \nabla^2 T_{\text{p}} \tag{11}$$

where T_{p} is the propellant temperature. λ_{p}, ρ_{p}, and c_{p} represent the thermal conductivity, density, and specific heat of the propellant, respectively.

The conjugate heat transfer calculation is realized by ensuring a consistent heat flux at the coupling interface between fluid and solid phase domains. The boundary condition at the interface is specified as follows:

$$-\lambda_{\text{p}}\left(\frac{\partial T_{\text{p}}}{\partial n}\right)_{\text{wall}} = h(T_{\text{g}} - T_{\text{w}}) \tag{12}$$

where h is the convective heat transfer coefficient, T_{w} and T_{g} are the temperatures of the propellant surface (coupling interface) and the adjacent gas-phase grid, respectively. The right-hand of the equation represents the heat flux from the gas to the propellant by convection.

It is assumed that the physicochemical processes of propellant combustion take place in a very thin layer on the propellant surface, and the chemical reactions between the propellant and gases are ignored. In addition, the influence of condensed particles in the combustion products is also ignored. The equivalent source term method is adopted to simulate the

mass-adding process of the burning propellant surface. According to the ignition temperature criterion described above, once the propellant surface temperature in one cell exceeds the critical ignition temperature T_c, the adjacent gas-phase grid will be taken as an added-mass cell. The combustion gas will be added into the flow field as source terms of the governing equations Eqs. (1)–(4) along the normal direction of the burning surface, as shown in Fig. 1. The detailed contents of the mass, momentum, and energy source terms are as follows:[14–16]

$$\begin{cases} S_m = \rho_p \dot{r} A_b / V_c \\ S_f = \rho_p \dot{r} A_b v_g / V_c, v_g = -\dot{r}\rho_p/\rho_g \\ S_h = \rho_p \dot{r} A_b c_g T_g / V_c \end{cases} \tag{13}$$

where $\dot{r}$ is the burning rate of the propellant. A_b and V_c denote the burning surface area and volume of the added-mass cell, respectively. v_g is the gas velocity of the added-mass cell along the normal direction of the propellant surface. ρ_g, c_g, and T_g are the density, specific heat at constant pressure, and temperature of the propellant gas, respectively.

The burning rate of the propellant is characterized by the modified Lenoir-Robillard's burning rate law,[6] in which the total burning rate $\dot{r}$ is treated as the superposition of the basic burning rate $\dot{r}_0$ and the erosive burning rate $\dot{r}_e$. The Vielle's burning rate law is used to describe $\dot{r}_0$, which is a function of the chamber pressure p. $\dot{r}_e$ represents the increase of the burning rate due to the erosive effect, and it is related to the heat convection between the gas flow and the propellant surface. The expression of $\dot{r}$ can be written as follows:

$$\dot{r} = \dot{r}_0 + \dot{r}_e = ap^n + \xi h_c \exp\left[-\beta \dot{r}\rho_p/(v_r\rho_r)\right] \tag{14}$$

where a and n denote the burning rate coefficient and pressure exponent of the propellant, respectively, ξ and β are constants determined by experiments, and h_c is the local convective heat transfer coefficient. v_r and ρ_r represent the gas velocity and density at the x_r section of the flow passage, respectively. Among that, x_r is the axial distance from the grain fore-end. The expression of h_c and the physical meanings of related parameters are detailed in Ref. 6.

3. Validation of numerical method

3.1. Solid propellant ignition case

To validate the developed solid propellant ignition and combustion model, the ignition start-up process of a laboratory-scale window SRM is numerically simulated. This case has been studied both experimentally and numerically by Peretz et al.[6] In the simulation setup of this study, the detailed parameters of the ignition gas, propellant grain, and motor structure are consistent with those in Ref. 6. Fig. 2 shows the comparison of the pressure histories at the motor fore-end obtained by experimental measurement and numerical simulation. It can be seen that the numerical results agree well with the experimental data. The predictions of the pressure rise rate and inflection point are very close to the experimental data, and the error of the peak pressure is less than 5%, indicating the validity of the numerical method for modeling the conjugate heat transfer, mass-adding, and pressure build-up in the chamber.

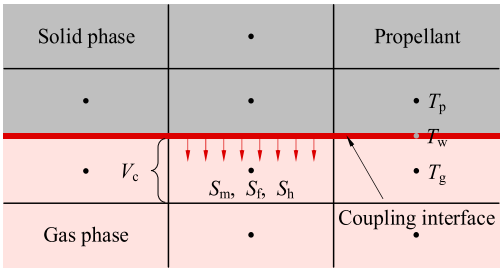


Fig. 1 Schematic diagram of propellant combustion and mass-adding.

3.2. Underwater supersonic gaseous jet case

To validate the numerical method for gas–liquid two-phase flow, a series of experiments have been conducted based on an experiment system of underwater supersonic gaseous jets. The experimental setup is shown in Fig. 3. A vertical pressurized water vessel with observation windows is used to construct a deep-water environment. The vessel is filled with water for a depth of 1 m in advance, and the air above the free surface in the vessel is pressurized by an air compressor and a gas tank to simulate the pressure of the required water depth. A pressure gauge is mounted on the side wall of the vessel to read the pressure inside it, as shown in Fig. 3(b). A central post is installed at the bottom of the vessel, and a Laval nozzle is mounted on the top of the central post through a threaded connection, as shown in Fig. 3(c). The nozzle throat diameter is 2 mm and the expansion ratio is 1.5625. Compressed air stored in a gas cylinder is used as the gas source in the experiment. When the solenoid valve is activated, the high-pressure air is injected vertically upwards into water through the nozzle. A high-speed camera (Phantom VEO 410L) is used to record the morphology evolution of underwater gas jets. Here, the sampling frequency is set to 10000 frame/s, and the captured images have a resolution of 640 pixel × 480 pixel.

In this case, the water depth set in the experiment is 100 m, and the total pressure at the nozzle inlet is 6.7 MPa. The vessel is inflated from the top gas inlet until the pressure gauge read-

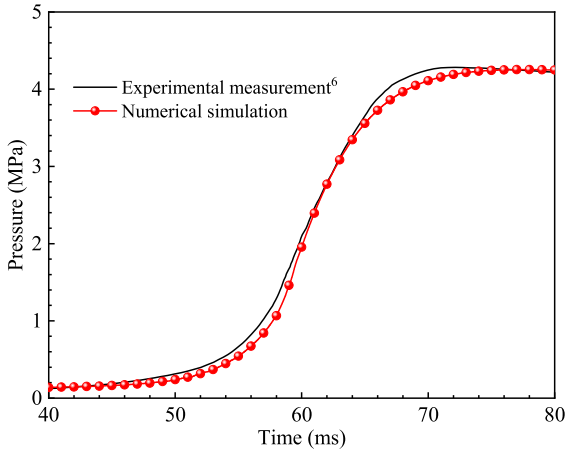


Fig. 2 Pressure histories at motor fore-end for experimental data and numerical results.

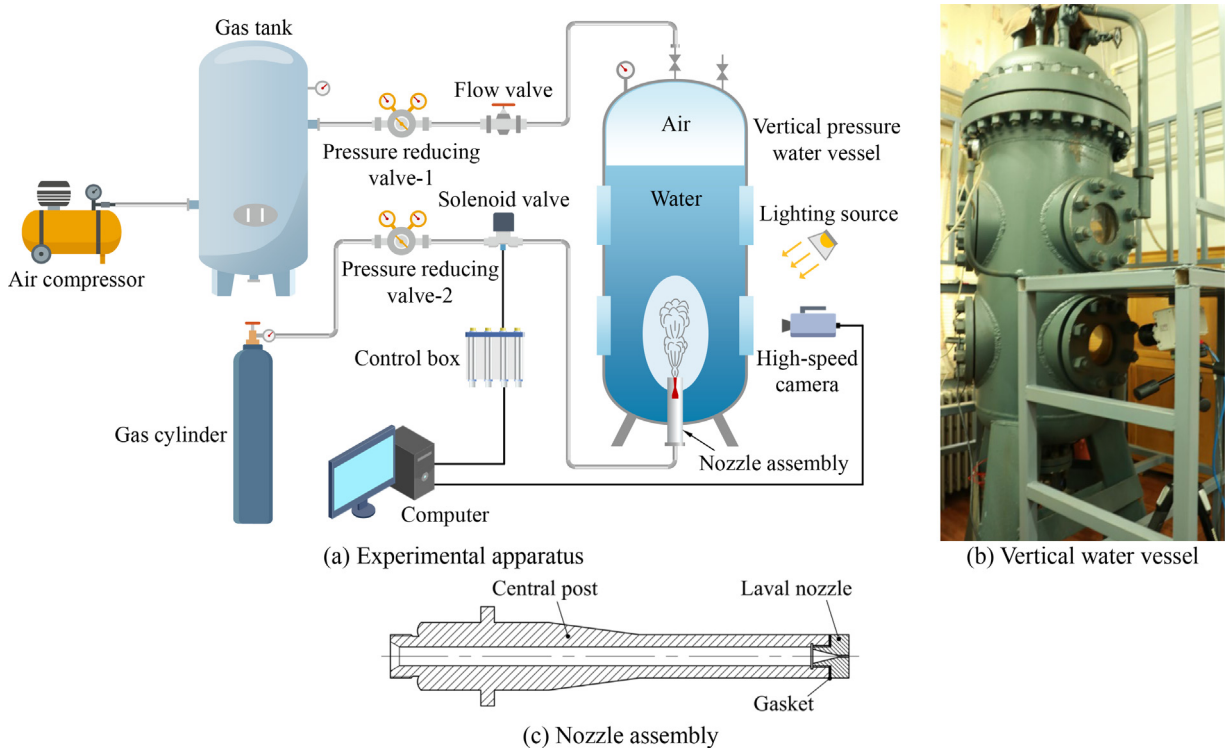


Fig. 3 Experimental setup for underwater supersonic gaseous jets.

ing reaches 1 MPa to meet the required test condition. The corresponding numerical simulation has also been conducted. Fig. 4 shows the comparison of the initial jet patterns at typical times obtained by numerical simulation and experimental photography. The contours of the gas-phase volume fraction α_g are given by the simulation results. It can be seen that the typical phenomena of underwater supersonic gas jets, such as necking, bulging, and back-attack, can be well reflected, and the variation rules of the gas–liquid interfaces and flow structures can be accurately captured by the numerical method. The morphology and size of the simulated jets are in good agreement with the experimental results, indicating the validity of the numerical method for simulating the underwater supersonic gas jets.

Fig. 5 compares the time histories of the jet penetration length obtained by experimental measurement and numerical simulation. Among that, the jet penetration length is defined

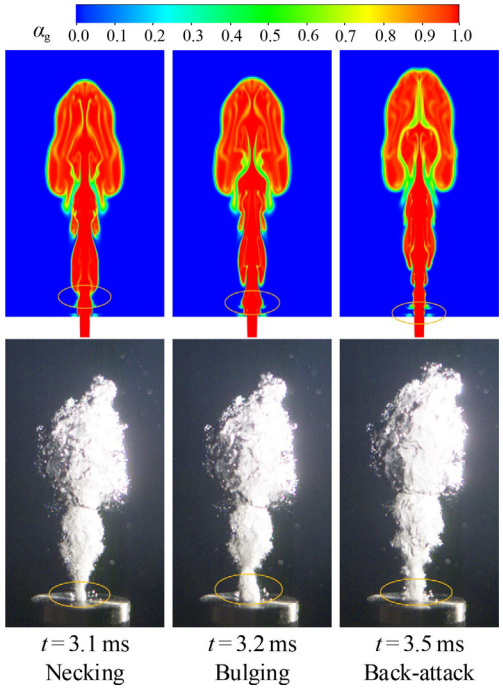


Fig. 4 Comparison of jet patterns obtained by simulation (up) and experiment[25] (down).

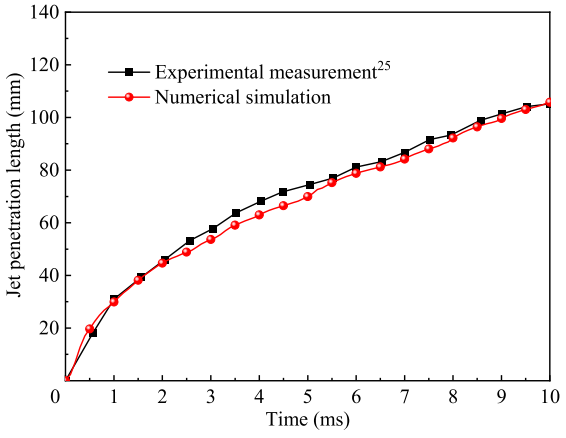


Fig. 5 Time histories of jet penetration length for experimental data and numerical results.

as the vertical distance from the nozzle outlet to the top of the gas boundary. It is noted that a good agreement is observed between experimental data and numerical results. Therefore, the developed numerical method is appropriate for studying the ignition start-up process of underwater SRMs in the later section.

4. Physical and computational models

4.1. Physical model

An underwater igniting SRM has been designed to study the ignition start-up process across a wide depth range. Fig. 6 shows the schematic of the designed motor, which consists of the igniter, steel case including the head-end plate and cylinder, solid propellant, combustion chamber, nozzle assembly, and nozzle closure. The igniter is enclosed in the center of the head-end plate, and the ignition gas can be injected from the side and top of the igniter. A simple internal-bore-burning tubular grain is used as the propellant grain, with an inner diameter of 64 mm, an outer diameter of 84 mm, and a length of 300 mm. A composite propellant with a low aluminum content is selected for the grain, and the propellant gas can be considered as a pure gas phase without particles. The throat and outlet diameters of the nozzle are 18 mm and 33 mm, respectively. The nozzle exit is equipped with a one-way opening sealing cover (nozzle closure) to prevent the entry of water from the external environment and accelerate the pressurization of the chamber. The nozzle closure will open instantaneously once the pressure difference between the inside and outside reaches 3 MPa. Zhang et al.[36] conducted underwater ignition experiments of an SRM in a large pressurized water vessel. To facilitate the validation and analysis in the later section, the nozzle structure and the closure-opening pressure difference of the present motor are consistent with those of the test motor in Ref. 36. Moreover, through a particular parametric design, the average rise rate of the chamber pressure during the initial start-up period is kept the same as that in Ref. 36.

4.2. Computational domain and mesh

An integrated model is constructed to achieve the coupled calculation of the flow field inside the motor and the flow field of the external underwater gas jets. Considering the axisymmetry of the physical model and economy in computing resources, a two-dimensional axisymmetric model is used for the numerical simulation. The computational domain consists of three parts: the solid propellant domain, the combustion chamber and nozzle domain, and the external water environment domain. The schematic diagram of the computational domain is shown in Fig. 7, where the internal and external flow domains of the motor are separated by the nozzle closure. For modeling the opening of the nozzle closure, the processes of deformation and separation are ignored, and the closure is simplified as an interior interface that can be switched instantaneously from solid to fluid. The distance from the right border of the external flow domain to the nozzle outlet is about $50R_e$ (R_e denotes the radius of the nozzle outlet) to ensure full development of the gas jets. The center of the nozzle exit plane is selected as the coordinate origin.

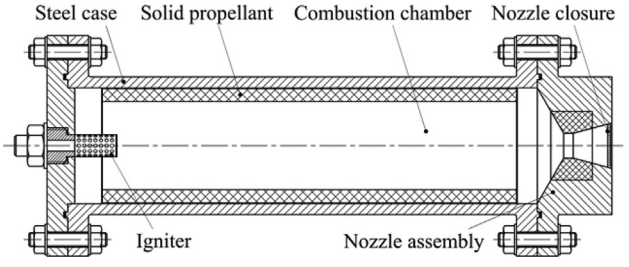


Fig. 6 Schematic of underwater igniting solid rocket motor.

Fig. 8 shows the computational mesh for the main regions of concern. Considering the short duration of the ignition start-up process, only the part near the burning surface is considered in the meshing of the solid propellant domain to save computing resources. The mesh is refined in regions with great variations in flow parameters, such as the nozzle, jet core, and walls, to better capture the flow details and meet the requirements of y^+ for the turbulence model. To eliminate the influence of the grid on the numerical results, three sets of computational grids with different cell numbers are generated for the grid independence study, namely 201072 (coarse grid), 260926 (medium grid), and 348961 (fine grid).

4.3. Boundary/initial conditions

Fig. 7 shows the boundary conditions for the computational domain, which are set based on the simulations for the ignition transient of an SRM in Ref. 9 and the underwater supersonic gas jets in Ref. 27. The computational parameters of the propellant and combustion gas used in the present model are given in Table 1. The outer surface of the igniter is defined as a mass flow inlet boundary with a prescribed typical mass flow rate[9,44] (as shown in Fig. 9) and ignition gas temperature. The ignition gas injected by the igniter is assumed to have the same physicochemical properties as the propellant gas. The inner surface of the tubular propellant grain is set as a conjugate heat transfer interface. In addition, the influence of the propellant regression is ignored due to the short duration of the ignition start-up process. The interior interface of the nozzle closure is regarded as an adiabatic solid wall before ignition. The area-averaged pressures on both sides of this surface are monitored during the simulation. Once the pressure difference reaches 3 MPa, this interior solid interface will be turned into an interior fluid interface. The left, upper, and right borders of the external water environment domain are defined as pressure outlet boundaries. All other walls are defined as non-slip adiabatic wall boundaries.

For the initial condition, the internal flow domain is defined as the gas phase with an initial pressure of 101325 Pa. The initial medium inside the motor is also assumed to have the same properties as the propellant gas. The external flow domain is defined as the liquid phase with an initial pressure of the hydrostatic pressure p_a corresponding to the water depth H. The value of p_a is calculated by the equation $p_a = p_{atm} + \rho_w g H$. Among that, p_{atm} is the atmospheric pressure at sea level, and ρ_w is the density of water. The flow field has an initial temperature of 300 K for both the fluid field and the propellant grain, and initially all components of the velocity are set equal to zero.

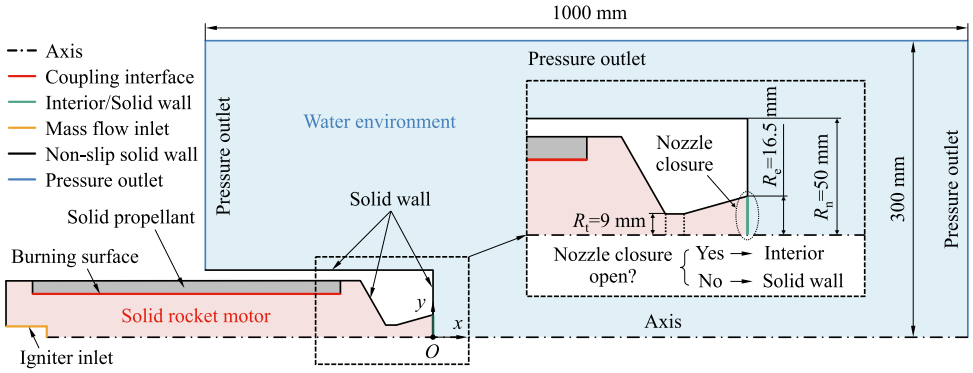
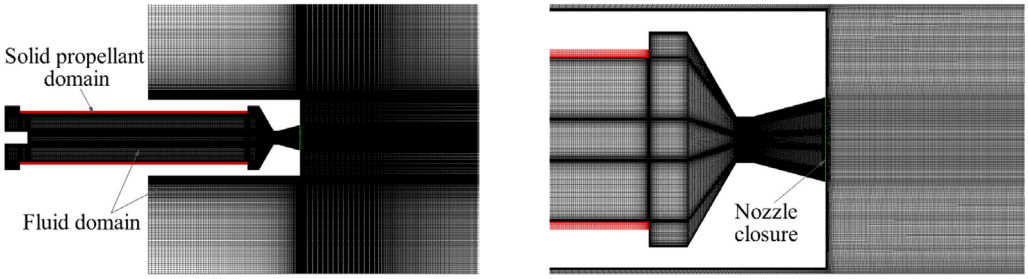


Fig. 7 Computational domain and boundary conditions.



(a) Mesh of motor and jet near-field (b) Mesh near nozzle

Fig. 8 Part of computational mesh (mesh is mirrored for purpose of clarity).

Table 1 Parameters for simulation of ignition transient.

Parameter	Value
Density of propellant ρ_p (kg/m^3)	1700
Thermal conductivity of propellant λ_p (W·m^{-1}·K^{-1})	0.25
Specific heat of propellant c_p (J·kg^{-1}·K^{-1})	1450
Burning rate coefficient a (m·s^{-1}·Pa^{-n})	2.5716×10^{-5}
Burning rate pressure exponent n	0.38
Critical ignition temperature of propellant T_c (K)	700
Temperature of propellant gas T_g (K)	3000
Specific heat ratio of propellant gas γ	1.234
Molecular weight of propellant gas M_g (kg/mol)	25
Temperature of ignition gas T_{ig} (K)	2600

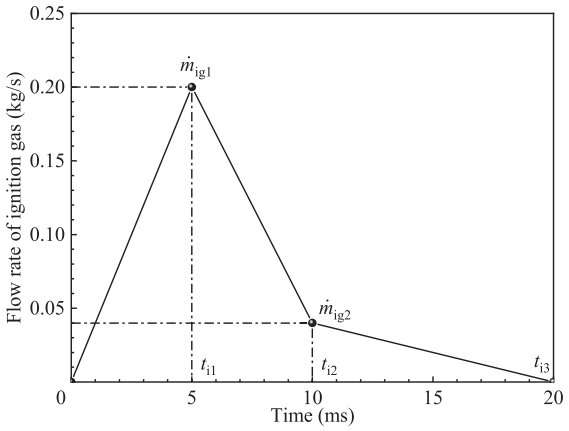


Fig. 9 Variation of mass flow rate at igniter inlet.

4.4. Simulation setup and procedure

The finite volume method is employed to solve the governing equations, and the coupling equations of pressure and velocity are solved with the SIMPLE algorithm. For the discretization in space, the gradient adopts the Green-Gauss node-based scheme, and the body force weighted scheme is applied for the pressure term. The density and momentum terms adopt a second-order upwind scheme, and the QUICK scheme is used for the phase volume fraction. A time step of 1×10^{-6} s is chosen for the simulation from the time step independence study. Fig. 10 illustrates the computational flow chart for the ignition start-up process of the underwater SRM. All of the simulations are performed using the commercial software FLUENT coupled with the User-Defined Function (UDF) codes.

Five operating conditions have been numerically simulated to comprehensively analyze the ignition start-up process of the underwater SRM across a wide depth range. Particularly, a sea-level air condition (Case-0) is considered to reveal the effect of environmental medium, and a relatively extreme condition for a depth of 100 m (Case-4) is considered to help understand the operating characteristics of SRMs in deeper water. The atmospheric pressure at sea level is taken as 0.1 MPa. According to the equation $p_a = p_{atm} + \rho_w g H$, it is approximated that the ambient pressure increases by 0.1 MPa for every 10 m increase in water depth. Thus, the closure-opening pressure p_o can be obtained for different depth

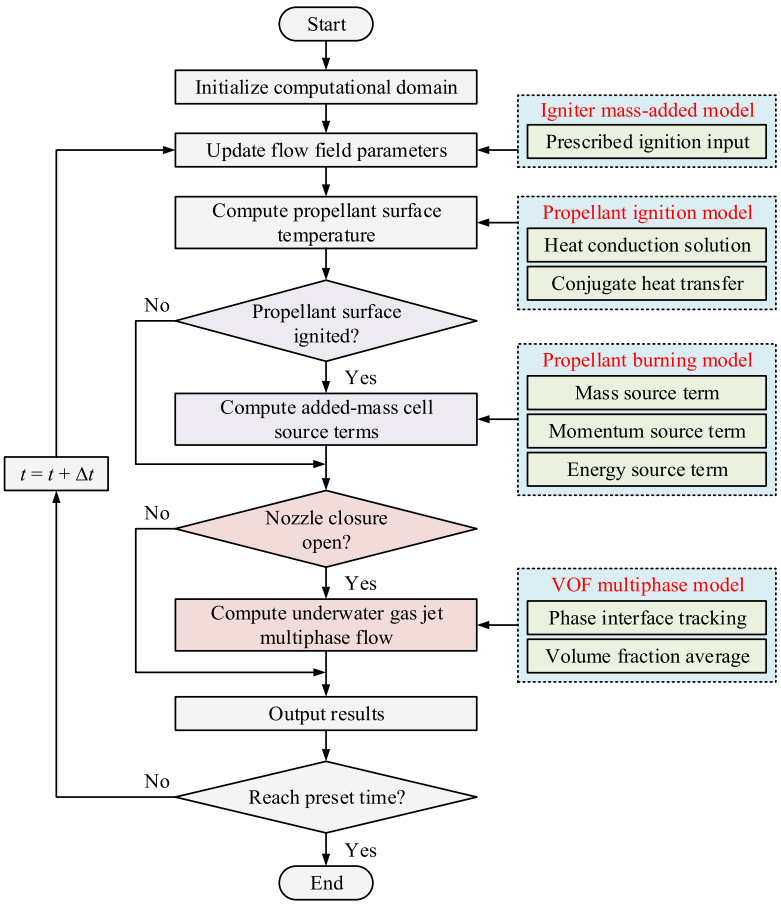


Fig. 10 Computational flow chart for ignition start-up process of an underwater solid rocket motor.

conditions. The parameter settings for different simulation conditions are shown in Table 2.

5. Results and discussion

5.1. Grid independence study

The grid independence study is conducted through numerical simulations of the ignition start-up process at a water depth of 10 m using the aforementioned three set grids. The numerical results at 12 ms after the opening of the nozzle closure are analyzed here. Fig. 11 shows the distributions of pressure (p) and Mach number (Ma) from $x = -0.1$ m to $x = 0.3$ m along the axis of the computational domain. The results clearly indicate that the medium and fine grids are nearly identical. Therefore, the medium grid is chosen for the follow-up simulations under a comprehensive evaluation of computing accuracy and economy in resources.

5.2. Flow field and internal ballistic characteristics of combustion chamber

Due to the sealing of the nozzle closure, the operating environment has no influence on the propellant combustion and gas flow inside the chamber before the closure opens. Fig. 12 shows the evolution of the temperature and pressure fields in the chamber. It can be seen that once the igniter is activated, the ignition gas is injected and flows along the gas passage. The inner surface of the propellant grain is continuously heated. Due to the direct impingement of the igniter jet flow, the grain fore-end is the first to reach the critical ignition temperature and be ignited, as shown in Fig. 12(b). Under the

Table 2 Operating conditions of simulation cases.

Case No.	0	1	2	3	4
Water depth H (m)	0 (air)	10	30	50	100
Ambient pressure p_a (MPa)	0.1	0.2	0.4	0.6	1.1
Closure-opening pressure p_o (MPa)	3.1	3.2	3.4	3.6	4.1

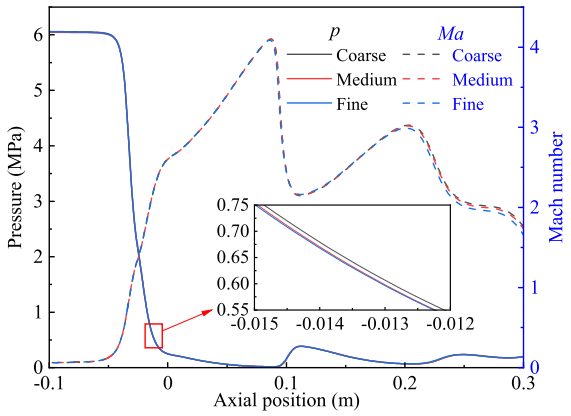


Fig. 11 Distributions of pressure and Mach number along axis for three different grids.

combined heating of the ignition gas and propellant gas, the flame rapidly spreads downstream until the entire exposed propellant surface is ignited, as shown in Fig. 12(d). With the continuous filling and accumulating of the gas, the overall level of the chamber pressure continues to rise. At about 7.6 ms, the maximum pressure value in the chamber reaches up to 3.09 MPa. As can be seen from Fig. 12, the pressure at the head and aft-end of the motor alternates between high and low values before the closure opens. This is because the upstream gas flow squeezes the gas in the passage to form compression waves, which spread along the passage and reflect at the nozzle wall and closure, resulting in oscillations of the pressure field.

To quantitatively evaluate the ignition performance, the time taken from the igniter operation until the chamber pressure reaches 75% of the equilibrium pressure p_{eq} is defined as the ignition delay time Δt.[45] Among that, the ignition induction period Δt_1 is the time from the igniter operation to the first ignition of the propellant surface; the flame-spreading period Δt_2 is the time from the first ignition of the propellant surface to the ignition of the entire propellant grain; the remaining time is the chamber-filling period Δt_3. To determine the values of Δt_1 and Δt_2, the time of the first ignition and the full ignition are obtained based on the time history of the propellant burning surface area, which is calculated synchronously in the simulation. In the present study, the equilibrium pressure of the chamber is designed to be 7.5 MPa. The internal ballistic characteristics of the motor in the air (Case-0) and at a depth of 10 m (Case-1) are compared in Fig. 13, where Fig. 13(a) shows the pressure histories of the chamber and nozzle outlet, and Fig. 13(b) shows the time history of the chamber pressure rise rate. Here, the chamber pressure is the volume-averaged pressure in the domain of the combustion chamber, and the nozzle outlet pressure is the area-averaged pressure in the nozzle outlet surface (i.e., the inner surface of the closure). It can be seen that the internal ballistic characteristics of the motor before the closure opens are the same, with Δt_1 and Δt_2 of 2.52 ms and 3.31 ms, respectively. After the propellant is ignited, the burning surface area and gas generation rate increase rapidly, resulting in a sharp rise in the chamber pressure and its rise rate.

The influence of the environmental medium on the internal ballistic characteristics is reflected after the closure opens. Compared with the air environment, the opening moment of the closure is delayed by 1.04% at a depth of 10 m due to the higher critical opening pressure p_o. As a result, the chamber pressure in the initial period after the closure opens is slightly higher, and the ignition delay time is shortened by 1.92%. Note that the difference between the chamber pressure curves becomes smaller as time goes on. This is due to the fact that the choked nozzle throat isolates the influence of the external environment, causing the chamber pressure to gradu-

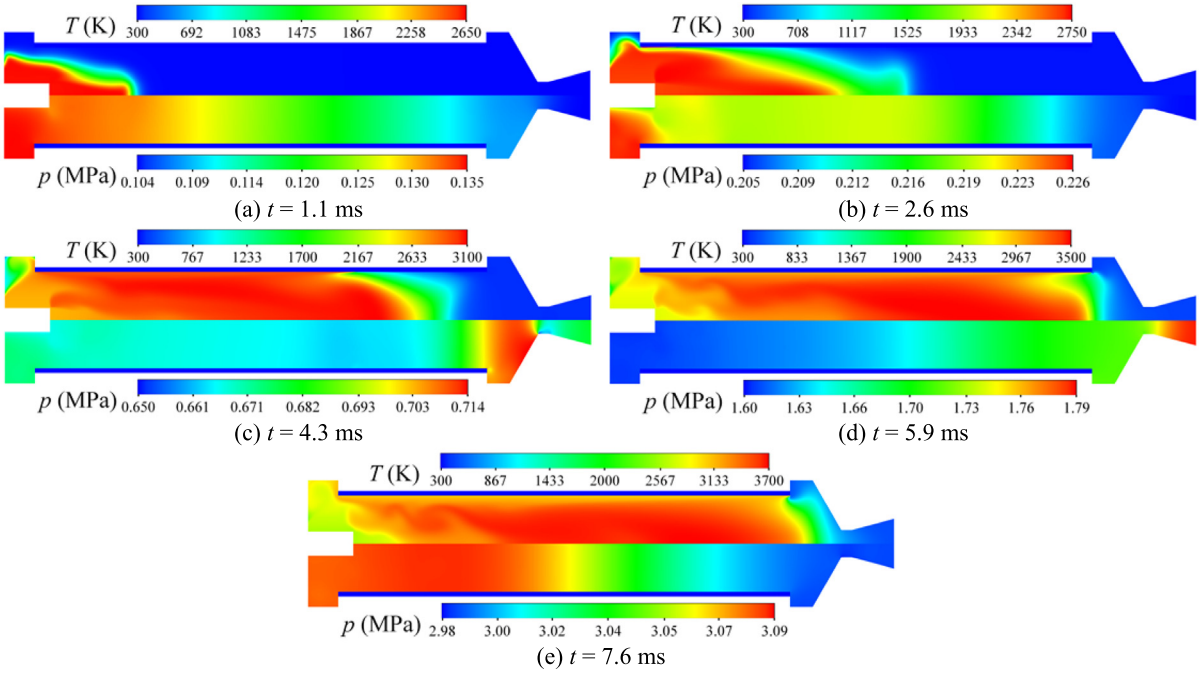
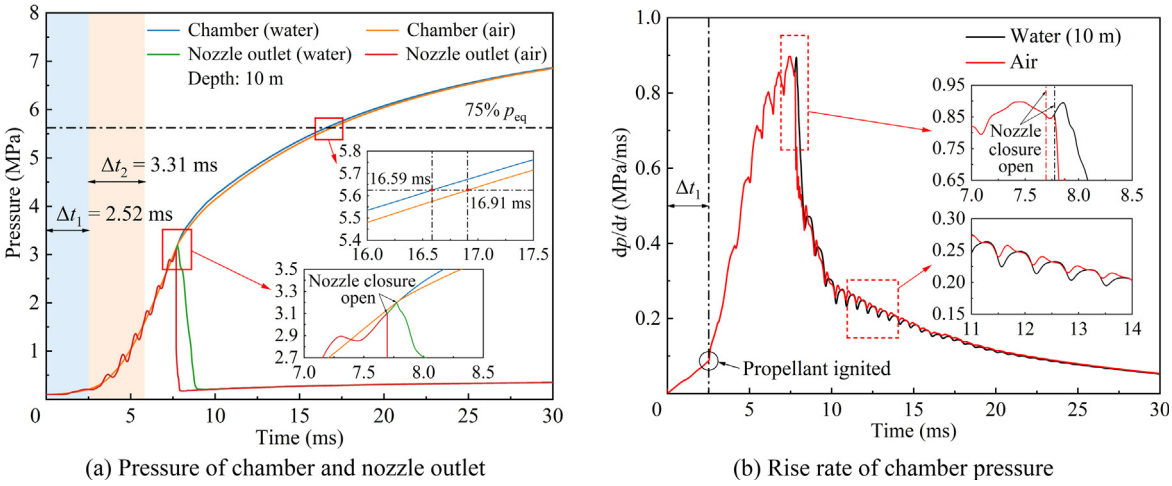


Fig. 12 Temporal variations of temperature and pressure fields in chamber before closure opens.



(a) Pressure of chamber and nozzle outlet (b) Rise rate of chamber pressure

Fig. 13 Internal ballistic characteristics of motor in air and at a water depth of 10 m.

ally approach the equilibrium value. After the closure opens, the nozzle outlet pressure and the rise rate of the chamber pressure decrease sharply. Meanwhile, as can be seen from Fig. 13(a), the nozzle outlet pressure decreases more slowly in the water environment. This is related to the hysteresis in the evolution of the nozzle flow field and will be discussed in Section 5.3.

The time histories of the chamber pressure at different water depths are shown in Fig. 14. It can be seen that the deeper the water depth, the higher the chamber pressure in the initial closure-opening period and the shorter the ignition delay time. Compared with the air environment, the opening moments of the closure are delayed by 1.04%, 2.34%, 7.28%, and 14.19% at depths of 10 m, 30 m, 50 m, and 100 m, respectively. Obviously, although the critical opening pressure of the closure increases linearly with the water depth, the opening moment of the closure does not vary linearly due to the pressure oscillations on the closure inner surface. As time goes on, the chamber pressure curves at different depths are gradually approaching. It can be deduced that, provided the ambient pressure meets the thermodynamic conditions of choked flow at the nozzle throat, the combustion and flow inside the chamber are largely unaffected by the variation of water depth during the steady operation stage.

Fig. 15 summarizes the variation rules of the motor ignition performance under different environmental conditions. It can be seen that as the depth increases, the proportion of the closure-opening moment t_o in the ignition delay time Δt gradually increases, and the decrease of Δt is significantly greater than the increase of t_o. The results indicate that the sealing stage of the closure contributes more to the pressure build-up process due to the higher rise rate of the chamber pressure. Therefore, it can be concluded that the influence of the operating environment on the internal ballistic characteristics during the ignition start-up process is realized by changing the opening moment of the closure. In deeper water, the combustion chamber can get into the steady operation state more quickly.

5.3. Flow structure evolution of underwater gas jets

After the nozzle closure opens, the high-pressure combustion gas is injected into the water environment, forming the supersonic gas jet. Fig. 16 presents the morphology of the exhausted gas bubble at 9 ms after the closure opens at a depth of 10 m. Among that, Fig. 16(a) is the numerical simulation result,

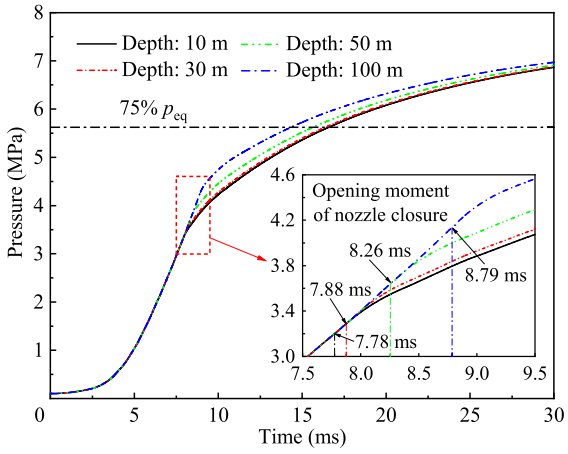


Fig. 14 Time histories of chamber pressure at different water depths.

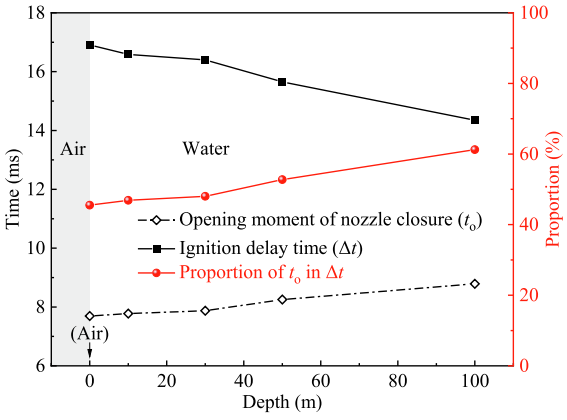


Fig. 15 Variation rules of motor ignition performance under different environmental conditions.

which shows the contour of gas volume fraction α_g; Fig. 16(b) is the experimental photography result in Ref. 36, where the red lines represent the outline of the motor structure. By comparison, it can be seen that the shape and size of the simulated gas bubble are basically consistent with the experimental result, despite the slight difference in the bubble axial length. This may occur due to the difference between the simulation treatment of the internal ballistics and the practical situation. In general, a satisfactory agreement between the numerical and experimental results is achieved, indicating the validity of the present integrated numerical model for the simulation of underwater ignition start-up process.

Fig. 17 shows the time history of the bubble vertex location at a depth of 10 m, as well as the bubble morphology evolution. The interface of two phases is plotted by the isoline with a gas volume fraction of 0.5. To facilitate the analysis, the opening moment of the closure is taken as the zero time. As shown in Fig. 17, within 11 ms after the closure opens, the gas bubble continues to expand axially and radially due to the continuous gas filling. However, the expansion rate in each direction is gradually slowing down. It can be seen that the present simulation results are in good agreement with the experimental data in Ref. 36. Moreover, in the simulation by Zhang et al.,[36] the detailed structure of the chamber is ignored and treated as a pressure inlet boundary. In contrast, the present numerical model is closer to the real physical processes and allows for richer data.

The temporal variations of the bubble morphology and Mach number distribution at different ignition depths are shown in Fig. 18. Considering that the opening of the nozzle closure is a prerequisite for the formation of gas bubbles, the corresponding closure-opening moment t_o is taken as the time reference for each depth condition to facilitate the analysis of the flow structure evolution. It should be noted that t_o has different values at different water depths (as shown in Fig. 15). Fig. 18 shows the simulation results at 4 ms, 8 ms, and 12 ms after the closure opens (denoted as t_o + 4 ms, t_o + 8 ms, and t_o + 12 ms, respectively). It can be seen that due to the blocking effect of the dense water medium, the radial expansion of the gas bubble dominates in the initial closure-opening period. Afterward, the top of the gas bubble is pushed up under the impingement of the high-momentum supersonic jet core, causing the bubble to present a cap-like shape. Then, driven by the development of the jet core, the gas bubble is gradually elongated axially and moves downstream with the

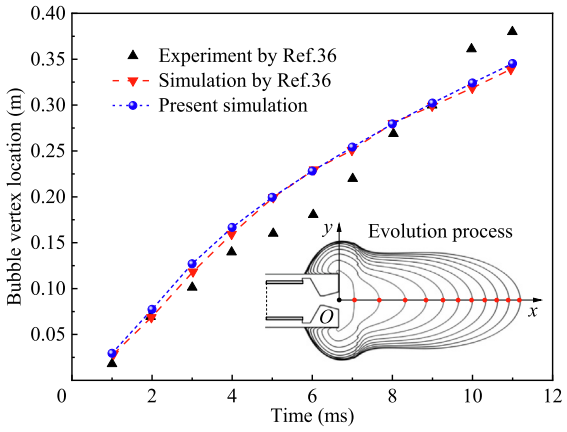
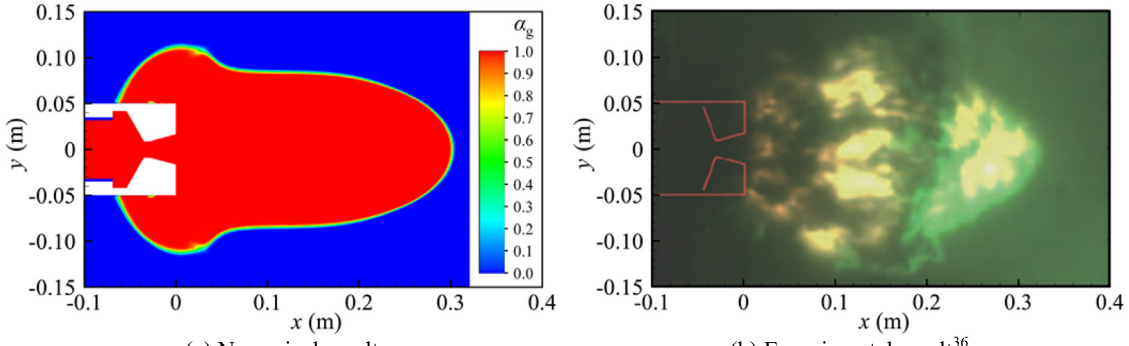


Fig. 17 Time history of bubble vertex location at a water depth of 10 m.

continuous gas filling, presenting an ellipsoidal shape. As the gas bubble gradually detaches from the motor aft-end, the bottom of the bubble gradually contracts inward, i.e., the first necking phenomenon occurs, forming a central gas passage and a separated gas bubble.

Before the first necking, due to the wrapping of the low-speed gas around the jet core, the length of the intercepting shocks at the nozzle outlet and the maximum Mach number increase as the chamber pressure rises, as shown in Fig. 18(a). After the formation of the central gas passage, due to the Kelvin-Helmholtz instability inherent to the high-speed gas–liquid shear flow,[46,47] there is unsteady turbulent mixing and entrainment at the interface of the gas passage. Under the interaction between the shocks and the unstable gas–liquid interfaces, the jet boundary near the nozzle outlet exhibits regular necking and bulging phenomena, resulting in oscillations of the shock position and Mach number, as shown in Figs. 18(c) and (d). As the water depth increases, the size of the gas bubble decreases at the same moment after the closure opens, and the first necking occurs earlier. Due to the rapid decay of the gas momentum, the separated gas bubble at the top is insufficient to resist the high-pressure ambient water, leading to irregular collapse of the morphology. In addition, as the water depth increases, the length of the jet core and the maximum Mach number decrease, and the intercepting shocks at the nozzle outlet gradually transform into the



(a) Numerical result (b) Experimental result[36]

Fig. 16 Morphology of gas bubble at 9 ms after closure opens at a water depth of 10 m.

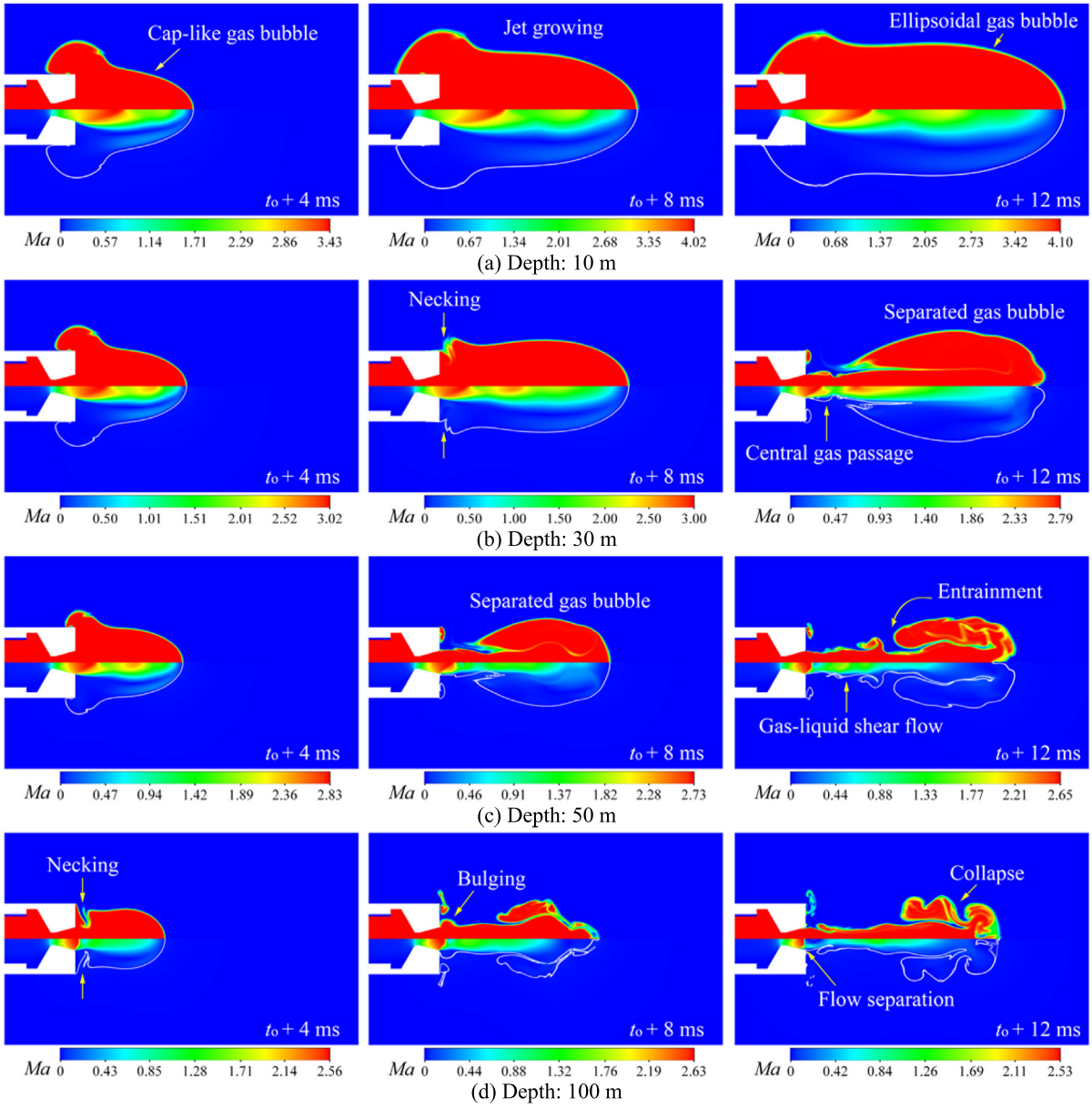
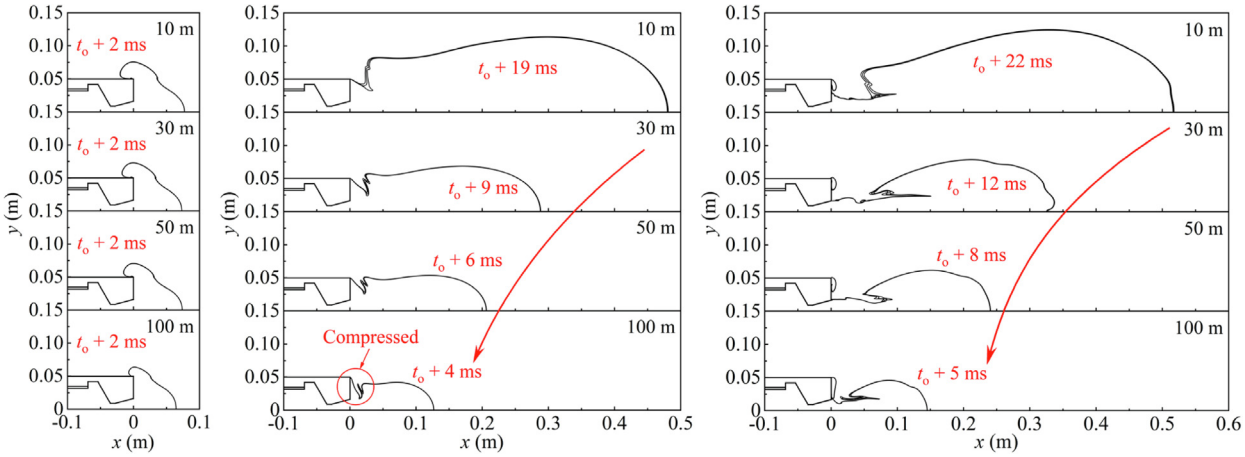


Fig. 18 Temporal variations of bubble morphology and Mach number distribution at different ignition depths.

intersecting oblique shocks containing a Mach disk. At a depth of 100 m, the nozzle is in a highly over-expanded state. The shocks are even pushed back into the divergent section of the nozzle, resulting in an extremely unstable operating mode with unwanted flow separation, as shown in Fig. 18(d).

To further analyze the effect of water depth on gas bubble evolution, three typical morphological patterns of the gas bubble can be defined based on the above description, namely initial expansion, first necking, and gas passage formation. Fig. 19 compares the occurrence time and morphology of the typical gas bubble patterns at different depths. It can be seen from Fig. 19(a) that there is little difference in the morphology of the gas bubbles at different depths at 2 ms after the closure opens. This is because the pressure difference for the opening of the closure is fixed, and the initial expansion of the gas bubble can be simplified as a free expansion movement driven by the pressure difference. Figs. 19(b) and (c) clearly show that with the increase of water depth and ambient pressure, both the axial and radial dimensions of the gas bubble decrease accordingly, and the occurrence time of the typical morphological patterns is advanced. It can be concluded that the deeper water environment brings significant compression and acceleration effects to the evolution of gas jets.

Fig. 20 compares the Mach number distributions of the gas jets at the same moment after the closure opens, both at a depth of 10 m and in the air. It can be seen that at 0.44 ms after the closure opens, the nozzle throat in water has just reached the critical state ($Ma = 1$), while in air a more complete shock structure has formed at the nozzle outlet. At 1.2 ms after the closure opens, the nozzle shock in water has just moved out of the divergent section, and the maximum Mach number increases to 2.6. However, the gas jet in air has fully developed,



(a) Initial expansion (b) First necking (c) Gas passage formation

Fig. 19 Comparison of occurrence time and morphology of typical gas bubble patterns at different water depths.

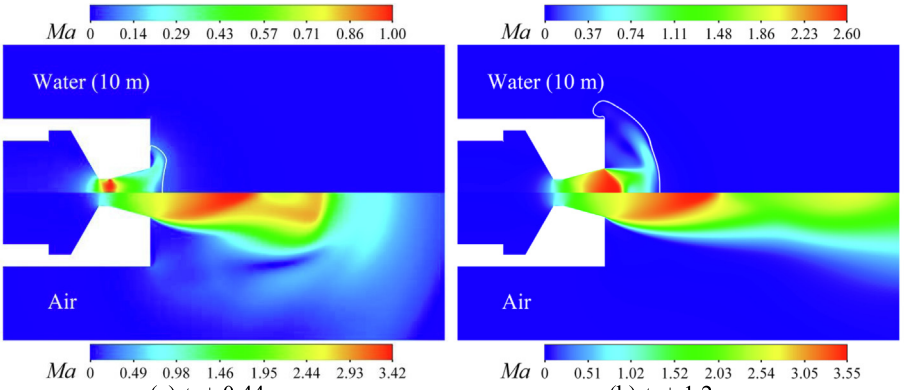
and the maximum Mach number increases by only 3.8%. Obviously, compared with the air environment, there is a significant lag in the evolution of gas jets in the water environment. This lag is mainly due to two reasons. One is that the high pressure at the nozzle outlet, generated by the strong gas impingement after the closure opens, weakens the thermodynamic conditions for the formation of the supersonic flow, which will be elaborated in Section 5.4. The other is that the blocking effect of the dense water medium slows down the gas exhaustion and the development of the shock structure.

5.4. Spatial and temporal characteristics of jet-flow pressure field

The temporal variations of Mach number distribution, pressure distribution, and gas–liquid interface within 1 ms after the closure opens at a depth of 10 m are shown in Fig. 21. It can be seen that at the moment of closure opening, the great pressure difference drives the gas to strongly impact the liquid phase, leading to a significant increase in the outlet pressure. The pressure waves propagate in the water-medium field and are reflected and superposed at the back wall of the motor, forming a fan-shaped high-pressure region. Under the blocking effect of the water, the gas first escapes along the edge of the nozzle outlet. Afterward, the gas bubble expands and develops rapidly in the radial direction, occupying the entire back wall. The transition from subsonic to supersonic flow in the nozzle is very obvious. The throat of the nozzle first reaches supersonic speed, forming a normal shock. Then, the normal shock gradually moves outward along the divergent section and evolves into an oblique shock structure with Mach reflection.

Fig. 22 shows the pressure distributions along the axis at different time after the closure opens at a depth of 10 m. It can be seen that at the very beginning of the closure opening, the pressure inside the nozzle varies a little, and the high pressure at the nozzle outlet generated by the gas impingement gradually decreases and approaches the ambient pressure. With the establishment of supersonic flow, a pressure valley first develops at the nozzle throat. After that, the expansion and acceleration of the gas causes the pressure to decrease rapidly along the axis, and a pressure peak appears again behind the shock. As time goes on, the length of the nozzle shock gradually increases due to the increasing chamber pressure. Thus, the low-pressure region near the nozzle outlet continues to expand, with the pressure peak gradually moving outward.

To further analyze the variation characteristics of the pressure field during the gas jet evolution, four probing points (P_1-



(a) t_o + 0.44 ms (b) t_o + 1.2 ms

Fig. 20 Mach number distributions of gas jets at same moment after closure opens in different environments.

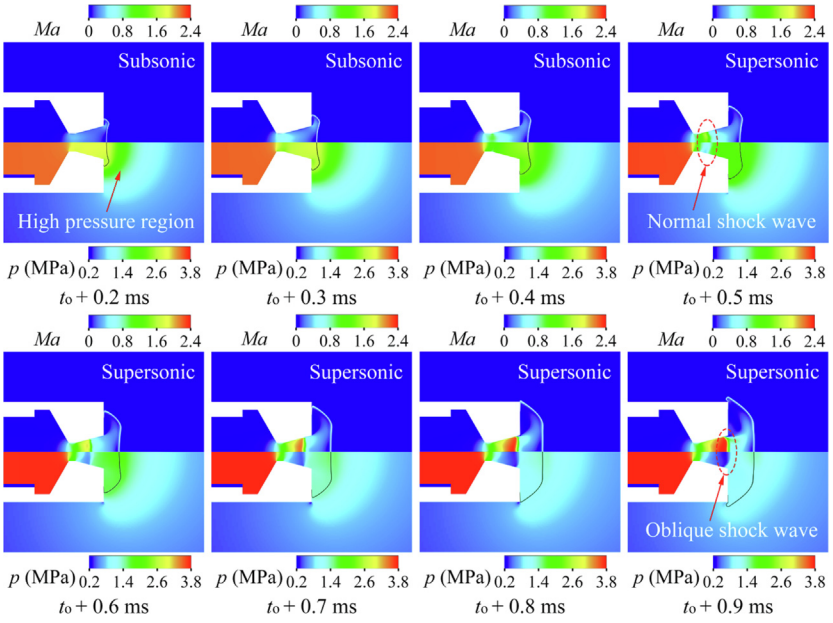


Fig. 21 Temporal variation of flow field near nozzle outlet within 1 ms after closure opens at a water depth of 10 m.

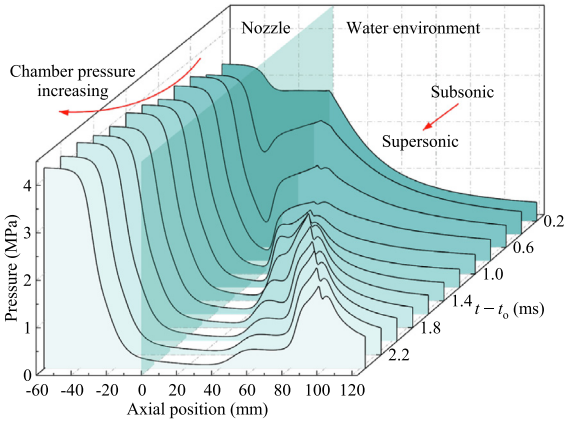


Fig. 22 Pressure distributions along axis at different time after closure opens at a water depth of 10 m.

P_4) are selected in the computational model. Among them, P_1 is located at the center of the nozzle exit plane, and P_2-P_4 are located on the back wall of the motor. The distribution of the probing points is shown in Fig. 23.

Fig. 24 shows the pressure histories of the probing points after the closure opens at different depths. Obviously, at the very beginning of the closure opening, the gas impingement causes the pressure at the probing points to be significantly higher than the ambient pressure, and the pressure level increases with the increase of water depth. As the gas expands fully, the pressure at P_1 continues to decrease. Note that due to the propagation of the pressure waves, the pressure at P_2-P_4 reaches a peak at about 0.4 ms after the closure opens and then decreases with the establishment of supersonic flow. Due to the damping effect of the pressure waves, the pressure level at the probing points decreases significantly along the radial direction, but the trends of the curves are similar. At about 1 ms after the closure opens, the shock moves out of the nozzle divergent section. As a result, the pressure at the probing points tends to be stable.

As can be seen from Fig. 24, after the first necking of the gas bubble, the pressure at the probing points begins to fluctuate. As the water depth increases, this fluctuation starts earlier and becomes more intense. This is because the intermittent necking and bulging of the jet boundary near the nozzle outlet cause the deformation of the shock structure, resulting in the fluctuation of the pressure field. In addition, the high ambient pressure brought about by the deep water intensifies this effect. It should be noted that the unsteady behaviors of the jet boundary have almost no influence on the pressure at P_1 with depths of 10 m, 30 m, and 50 m, since the shock is always located outside the nozzle. In contrast, the pressure at P_1 with a depth of 100 m is characterized by significant intermittent pulse-like oscillations. This is because the high ambient pressure causes the shock to be intermittently pushed back into the nozzle divergent section. The shock front sweeps back and forth through the point P_1, resulting in such pulse-like pressure oscillations.

Fig. 25 shows the pressure field and axial pressure distribution of the gas jet for typical necking and bulging moments at a depth of 50 m. It can be seen that the shock at the nozzle outlet causes the formation of low-pressure and high-pressure regions in the central gas passage. During necking, the squeezing of the jet boundary brings the shock closer to the nozzle outlet and increases its intensity. Meanwhile, the high pressure behind the shock leads to an increase of the pressure on the back wall, as shown in Fig. 25(a). During bulging, the expansion of the jet boundary lengthens the shock structure and reduces its intensity. The effect of the low pressure in front of the shock is more

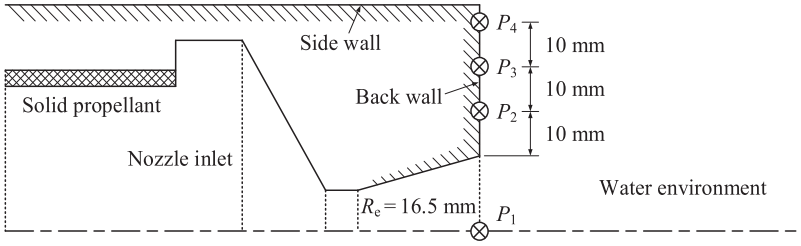


Fig. 23 Locations of pressure probing points.

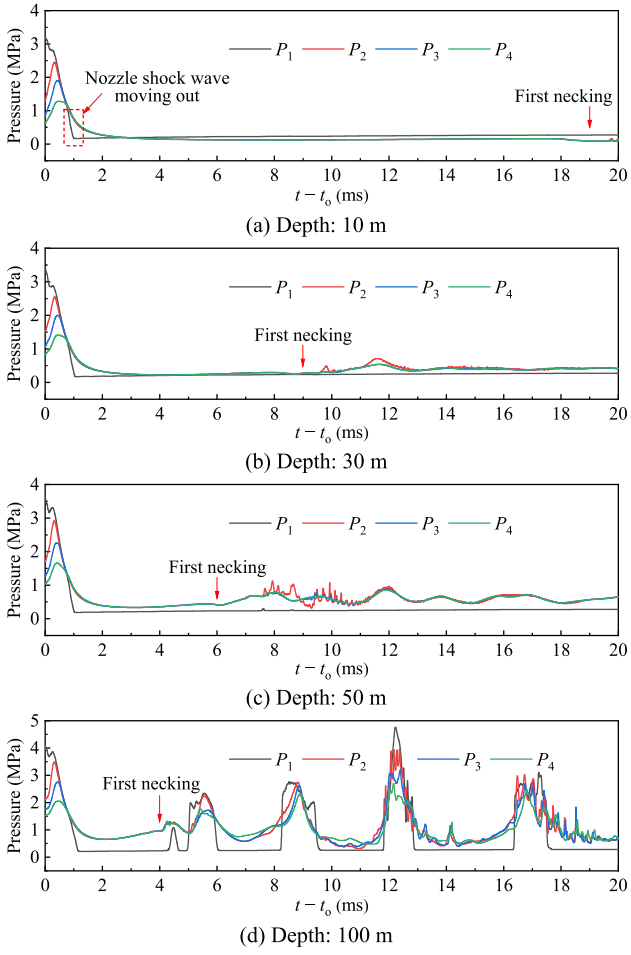


Fig. 24 Pressure histories of probing points after closure opens at different water depths.

dominant, leading to a decrease of the pressure on the back wall, as shown in Fig. 25(b). The change in the pressure field caused by the shock-structure deformation will feed back into the behavior of the jet boundary. Therefore, in general, the necking and bulging occur alternately, resulting in the fluctuation of the pressure field. As the depth increases, the shear effect of the high-speed gas–liquid flow and the shock/jet interface interactions become more intense, leading to more significant necking and bulging of the gas jet. Meanwhile, the amplitude of the pressure fluctuations is greater due to the stronger shock intensity.

5.5. *Effect of water depth on initial thrust performance*

Thrust is one of the most important performance parameters of an SRM. The pressures acting on the underwater SRM during operation are shown in Fig. 26. Here, p_c is the chamber pressure, p_n is the pressure on the nozzle wall, and p_b is the pressure on the back wall of the motor. A_c and A_s represent the cross-sectional areas inside and outside the chamber case, respectively. A_t and A_e represent the cross-sectional areas at the throat and outlet of the nozzle, respectively.

The thrust can be calculated by integrating the wall pressure. Considering the axisymmetry of the model, the radial thrust component is zero. Hence, the thrust F of the underwater SRM can be expressed as:[25]

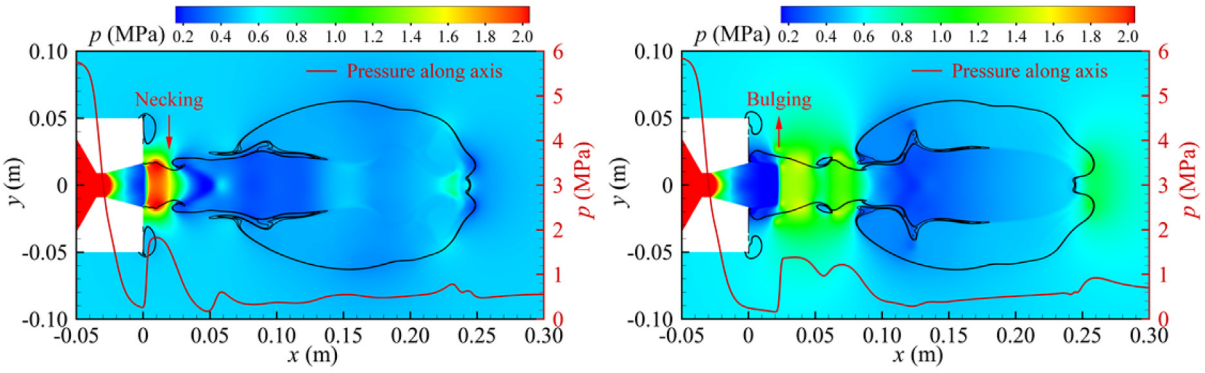
$$F = \int_{s_1} p_n \mathrm{d}A_x + \int_{s_2} p_b \mathrm{d}A_x + p_c A_c - p_a A_s \tag{15}$$

where s_1 denotes the nozzle wall, s_2 denotes the back wall, and A_x is the axial component of the area vector.

Unlike in air, the additional thrust caused by the pressure difference between the front and back walls of the motor is very obvious in water. Therefore, to facilitate the analysis, the thrust F is defined as the sum of the internal thrust F_{intl} and the external thrust F_{ext}. The thrust components can be written as follows:

$$\begin{cases} F_{intl} = \int_{s_1} p_n \mathrm{d}A_x + p_c A_c \\ F_{ext} = \int_{s_2} p_b \mathrm{d}A_x - p_a A_s \end{cases} \tag{16}$$

The thrust characteristics of the motor in the air and at a depth of 10 m are compared in Fig. 27, which indicates the effect of the environmental medium. Due to the reciprocating motion of the compression waves inside the chamber, there is a slight oscillation in the internal thrust. After the closure opens, this oscillation gradually weakens as the gas flow in the chamber tends to be steady. As can be seen from Fig. 27(a), compared with operating in air, the typical thrust characteristics of the SRM operating underwater include a significant initial thrust peak caused by gas impingement and thrust fluctuations caused by gas–liquid interactions. Despite the delayed response due to the flow evolution hysteresis at the beginning of the closure opening, the variation trend of the internal thrust at a depth of 10 m is very close to that in the air, as shown in Fig. 27(b). After the initial high pressure, the contin-



(a) t_o + 8.6 ms (b) t_o + 9.2 ms

Fig. 25 Pressure field and axial pressure distribution of gas jet for typical necking and bulging moments at a depth of 50 m.

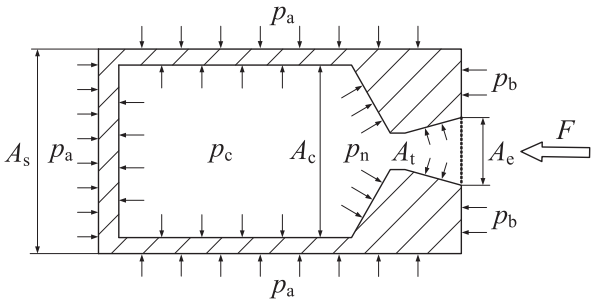
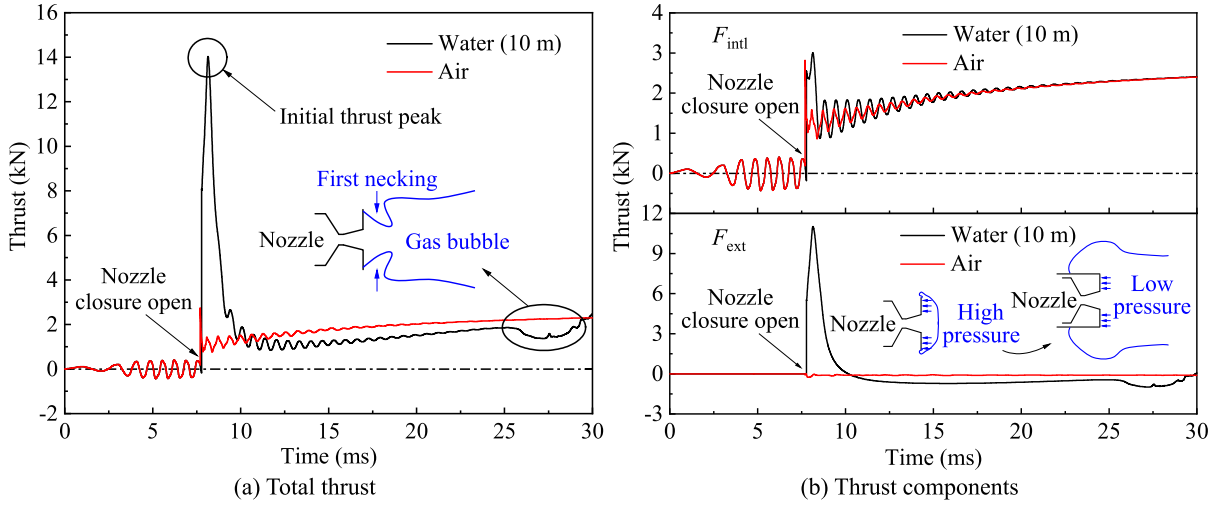


Fig. 26 Schematic diagram of thrust calculation principle.

uous decrease of the pressure on the back wall causes a negative external thrust, resulting in a reduction of the total thrust at a depth of 10 m. Moreover, with the occurrence of the first necking and subsequent movements of the jet boundary, there are also fluctuations in the external thrust. In contrast, the external thrust in the air is always close to zero.

Fig. 28 shows the thrust characteristics of the motor after the closure opens at different depths, including the total thrust, internal thrust, external thrust, and force on the back wall. Although the initial values of each thrust component are different at different depths, the initial peak of the total thrust is basically the same, with a peak of about 14 kN, as shown in Fig. 28(a). The force on the back wall directly determines the variation rules of the external thrust and total thrust. As the water depth increases, the pressure fluctuations on the back wall caused by the necking and bulging of the gas jet are intensified, resulting in increasingly significant fluctuations in the external thrust, echoing the results in Fig. 24. At a depth of 100 m, the fluctuations in the internal thrust also appear synchronously due to the intermittent high pressure on the nozzle wall brought about by the shock motion in the divergent section. However, at other depths, the internal thrust varies more smoothly with basically similar trends. It should be noted that at a depth of 100 m, the total thrust of the motor oscillates violently with intermittent negative values, which will result in an extremely low propulsive efficiency.

Fig. 29 shows the average values of total, internal, and external thrust within 20 ms after the closure opens at different water depths. It can be seen that as the depth increases, the average internal thrust gradually increases due to the higher



(a) Total thrust (b) Thrust components

Fig. 27 Thrust characteristics of the motor in the air and at a water depth of 10 m.

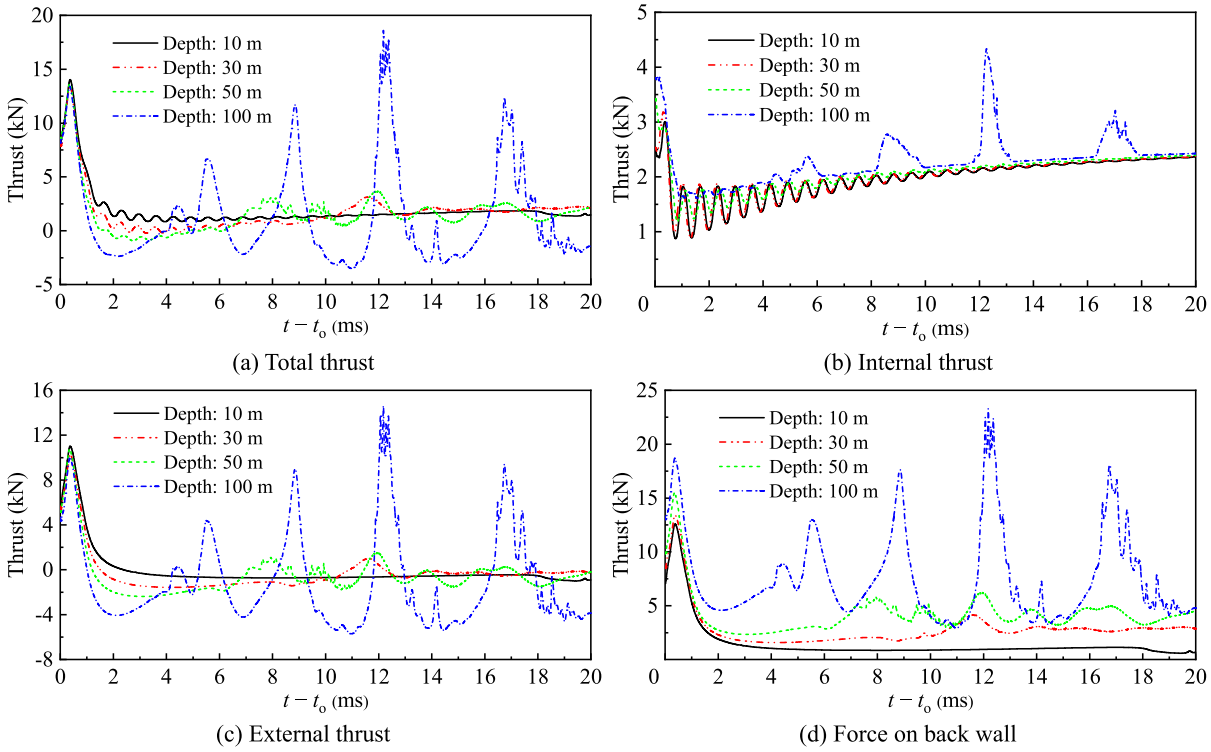


Fig. 28 Thrust characteristics of motor after closure opens at different water depths.

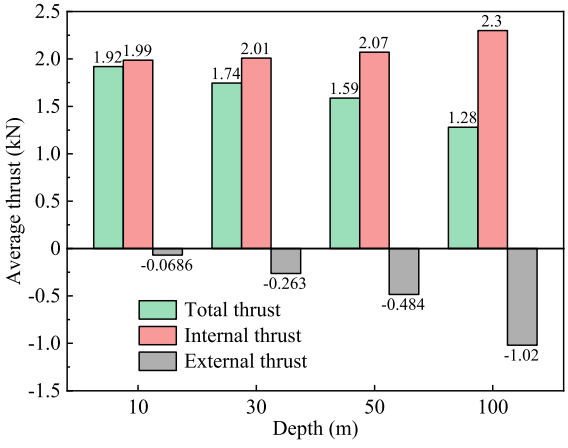


Fig. 29 Average thrust of motor within 20 ms after closure opens at different water depths.

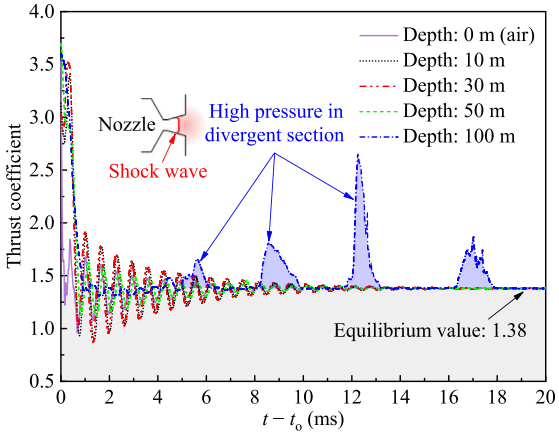


Fig. 30 Time histories of thrust coefficient after closure opens under different environmental conditions.

chamber pressure. At a depth of 100 m, this effect is enhanced by the fluctuations in internal thrust. For all depths, the average external thrust is negative due to the intermittent low pressure on the back wall. Moreover, the average value of the negative external thrust is greater in deeper water due to the earlier and more intense flow oscillations. This effect is more dominant than the increase in average internal thrust. As a result, during the initial start-up period, the average total thrust of the motor decreases with the increase of depth, which will negatively affect the propulsive efficiency and launch reliability of underwater vehicles in deep-water environments.

The external thrust is the resultant force of the pressure exerted on the motor outer surface, which can be regulated by hydrodynamic shape design. There have been some studies on the control of external thrust by optimizing the tail shape of the vehicle and improving the surface structure of the back wall.[48,49] In contrast, the internal thrust characterizes the quality of the gas expansion and the operating performance of the motor. To eliminate the effect of chamber pressure variation

on the internal thrust, a dimensionless thrust coefficient C_F is defined as:

$$C_F = F_{\text{intl}}/(p_c A_t) \tag{17}$$

Fig. 30 shows the time histories of the thrust coefficient after the closure opens under different environmental conditions. It can be seen that the thrust coefficients gradually become stable and tend to be the same for all conditions except 100 m depth, with an equilibrium value of about 1.38. At a depth of 100 m, the shock in the divergent section disrupts the normal expansion flow in the nozzle, and the high pressure behind the shock causes the thrust coefficient to increase significantly on the basis of the equilibrium value. Therefore, it can be concluded that provided the water depth is insufficient for the shock to be pushed back into the nozzle, the internal thrust generated by the motor has the same characteristics for different operating environments.

5.6. Correlation mechanism between flow characteristics and thrust oscillations

In deeper water, the oscillations of the flow parameters and motor thrust are more obvious. Here, the variation rules of the nozzle shock under the extreme condition of 100 m depth are carefully analyzed to reveal the correlation between flow characteristics and thrust oscillations. The Mach number distributions along the axis at different times after the nozzle throat reaches the critical state are obtained. Among them, the first Mach number peak (the point of maximum Mach number along the axis) occurs at the intersection of the nozzle shock and the axis, which can be used to characterize the shock position. At a depth of 100 m, the time histories of the axial position and value of the first Mach number peak are shown in Fig. 31.

As can be seen from the figure, the shock gradually moves outward along the divergent section and grows steadily in the initial period, since the back wall of the motor is wrapped by the gas bubble. After the high-speed jet core interacts with the water, large-amplitude motions of the nozzle shock begin to appear. The corresponding value of the Mach number peak also varies synchronously as the shock intermittently moves in and out of the divergent section. In the figure, t_1, t_2, t_3, and t_4 are several typical moments when the shock moves inward or outward to the limit position, respectively. It should be noted that the moments when the shock moves inward to the limit position (t_1, t_3, and t_4) coincide well with the peak moments of the internal and external thrusts in Fig. 28. Due to the instability of the gas–liquid interface and the compressibility of the gas, the energy accumulation from successive necking and bulging may lead to a large-amplitude oscillation, as shown at t_4. This phenomenon has also been reported in Ref. 20.

Fig. 32 shows the flow field structure and flow parameters along the axis at the typical moments at a depth of 100 m. It can be observed that the jet necking occurs at t_1, t_3, and t_4, while the jet bulging occurs at t_2. When the shock moves inward to the limit position, the gas flow behind the shock drops to subsonic speed. The necking of the jet boundary results in a significant narrowing of the central gas passage, and the low-speed gas accumulates in the bubble at the nozzle outlet, forming a high-pressure region. The high pressure from the shock to the necking position significantly increases the pressure on the divergent section wall and the back wall, resulting in a thrust peak. Moreover, the greater the amplitude of the shock moving inward, the higher the peak of the motor thrust. The high pressure generated by the necking leads to the subsequent expansion of the jet boundary. At t_2, the full expansion of the gas allows the formation of a supersonic jet core outside the nozzle. Meanwhile, the low pressure near the nozzle outlet causes a thrust valley.

It can be concluded that there is a strong coupling between the behavior of the jet boundary, the motion of the shock, and the variation of the pressure field. The wall pressure fluctuations lead directly to the thrust oscillations, and the first necking of the gas bubble triggers this cycle of instability. Furthermore, it can be observed that the inward motion of the shock leads to flow separation inside the nozzle. Note that gas–liquid separation may also occur at the shock separation point, as shown at t_3 and t_4. Given the fact that the flow separation inside the nozzle sometimes exhibits a loss of symmetry, the thrust oscillations may also be accompanied by unstable side loads.[50,51]

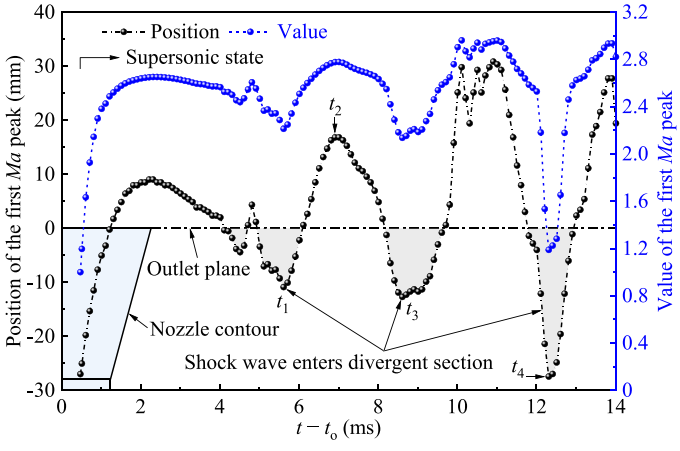


Fig. 31 Time histories of axial position and value of the first Mach number peak at a water depth of 100 m.

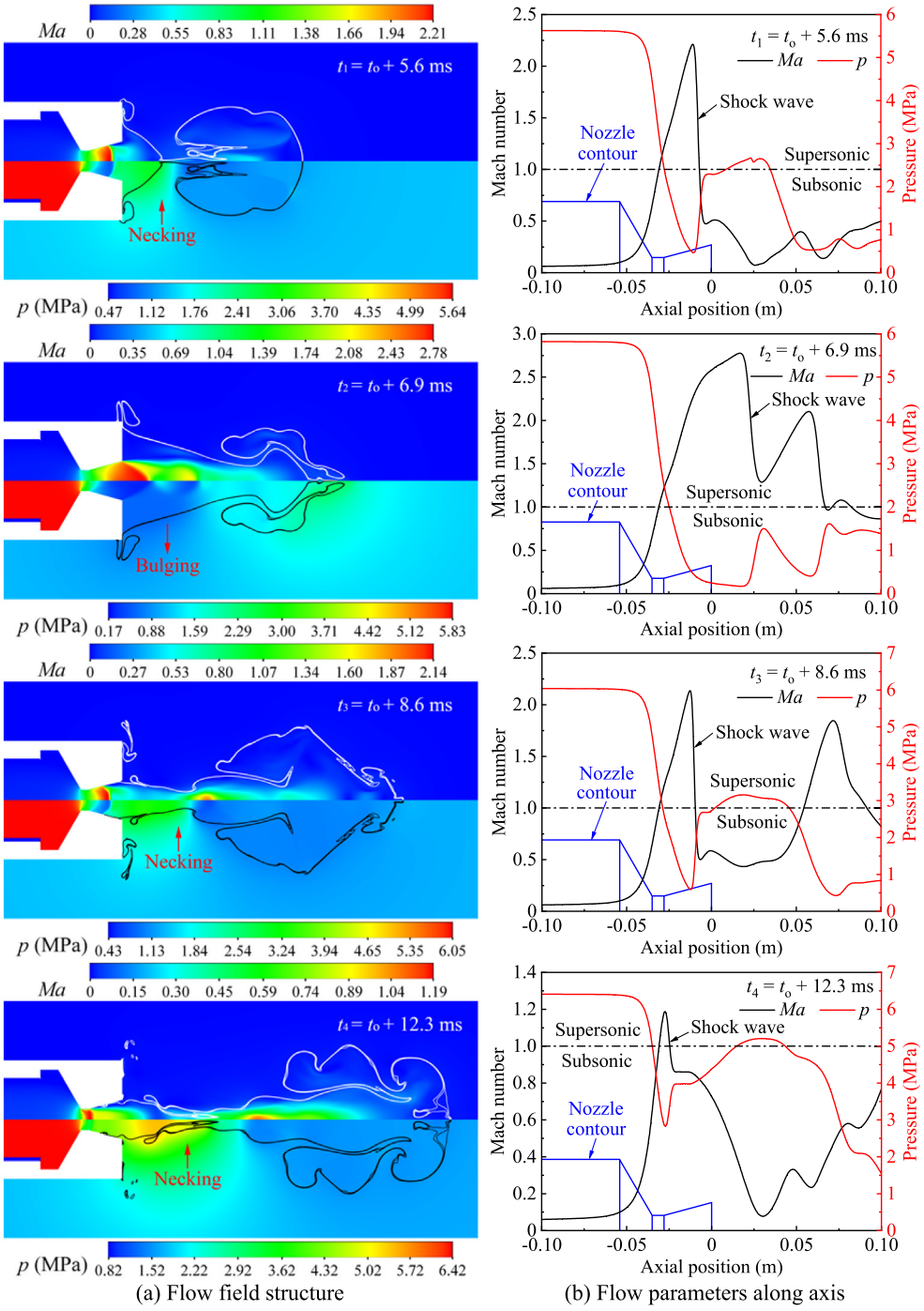


Fig. 32 Flow field structure and flow parameters along axis at typical moments at a water depth of 100 m.

6. Conclusions

In this paper, a multi-domain integrated model has been developed to numerically study the ignition start-up process of an underwater SRM across a wide depth range. The characteristics of the flow field developments, internal ballistics, and thrust oscillations are carefully analyzed. The effects of environmental medium and operating depth are systematically discussed. The conclusions are drawn as follows:

(1) The influence of the operating environment on the chamber pressurization process is primarily reflected in the initial period after the closure opens. As the water depth increases, the delay in the closure-opening moment increases, and so does the chamber pressure in the initial closure-opening period, leading to a shorter ignition delay time. Due to the choked nozzle throat, the chamber pressures gradually approach the same equilibrium value. After the closure opens, the high pressure at

the nozzle outlet generated by the strong gas impingement results in an initial thrust peak that is essentially the same at all depths.

(2) Due to the blocking effect of water, the development of the gas jet in water lags significantly compared with that in air. The deeper water environment brings significant compression and acceleration effects to the evolution of gas jets. However, there is little difference in bubble morphology during the initial closure-opening period. Under the interaction between the shocks and the unstable gas–liquid interfaces, the jet boundary exhibits intermittent necking and bulging phenomena, resulting in oscillations of the shock structure and flow parameters.

(3) There is a strong coupling between the behavior of the jet boundary, the motion of the shock, and the variation of the pressure field. As the depth increases, the pressure fluctuations on the back wall caused by the alternating necking and bulging of the gas jet are intensified, resulting in more significant oscillations in the external thrust. At a depth of 100 m, the shock is intermittently pushed back into the nozzle divergent section, and the oscillations in the internal thrust also appear synchronously. The greater the limit amplitude of the shock moving inward, the higher the peak thrust. During the initial start-up period, the average total thrust of the motor decreases with the increase of depth.

CRediT authorship contribution statement

Deyou WANG: Conceptualization, Formal analysis, Investigation, Methodology, Writing – original draft. **Shipeng LI:** Formal analysis, Funding acquisition, Project administration, Supervision. **Ge JIN:** Data curation, Formal analysis, Validation. **Ruyao WANG:** Investigation, Visualization, Writing – review & editing. **Dian GUAN:** Methodology, Software. **Ningfei WANG:** Resources, Supervision.

Declaration of competing interest

The authors declare that they have no known competing financial interests or personal relationships that could have appeared to influence the work reported in this paper.

Acknowledgements

This study was supported by the National Level Project of China.

References

1. Huang LY, Zhang WH, Xia ZX, et al. Experimental study on ignition process of a magnesium-based water ramjet engine. *J Propuls Power* 2014;**30**:857–62.
2. Liu DC, Li SL, Xie GN. Effect of primary water injection angle on thermal propulsion performance of a water ramjet engine. *Aerosp Sci Technol* 2020;**97**:105630.
3. Nguyen AT, Deniau H, Girard S, et al. Unsteadiness of flow separation and end-effects regime in a thrust-optimized contour rocket nozzle. *Flow Turbul Combust* 2003;**71**(1):161–81.
4. He MS, Qin LZ, Liu Y. Numerical investigation of flow separation behavior in an over-expanded annular conical aerospike nozzle. *Chin J Aeronaut* 2015;**28**(4):983–1002.
5. Ferguson JD. Experimental data from underwater conical nozzles exhausting N_2 gas. *J Hydronautics* 1969;**3**(4):200.
6. Peretz A, Kuo KK, Caveny LH, et al. Starting transient of solid-propellant rocket motors with high internal gas velocities. *AIAA J* 1973;**11**(12):1719–27.
7. Johnston WA. Solid rocket motor internal flow during ignition. *J Propuls Power* 1995;**11**(3):489–96.
8. Johnston W, Murdock J. Flow-structural interaction inside a solid rocket motor during ignition transient. *J Propuls Power* 1995;**11**(5):998–1005.
9. Hu BW, Wang B, Tian XT. Numerical modeling and studies of ignition transients in end-burning-grain solid rocket motors. *J Propuls Power* 2016;**32**(6):1333–42.
10. Favini B, Zaghi S, Serraglia F, et al. 3D numerical simulation of ignition transient in SRM. *42nd AIAA/ASME/SAE/ASEE joint propulsion conference and exhibit*. Reston: AIAA; 2006.
11. Ajith S, Nichith C, Vignesh S, et al. 3D Flame spread and starting transient in dual-thrust solid propellant rocket motors. *52nd AIAA/SAE/ASEE joint propulsion conference*. Reston: AIAA; 2016.
12. Han S, Kim C. Integrated fluid–structure simulation for full burning of a solid-propellant rocket interior. *J Propuls Power* 2014;**30**(4):883–900.
13. Li Q, Liu PJ, He GQ. Fluid-solid coupled simulation of the ignition transient of solid rocket motor. *Acta Astronaut* 2015;**110**:180–90.
14. Li YK, Han JL, Chen X, et al. Numerical simulation of the ignition transient of dual pulse motor based on multi-physics coupling. *Acta Aeronautica et Astronautica Sinica* 2017;**38**(4):120409 [Chinese].
15. Li YK, Chen X, Xu JS, et al. Three-dimensional multi-physics coupled simulation of ignition transient in a dual pulse solid rocket motor. *Acta Astronaut* 2018;**146**:46–65.
16. Li YK, Chen X, Cheng HG, et al. Fluid–structure coupled simulation of ignition transient in a dual pulse motor using overset grid method. *Acta Astronaut* 2021;**183**:211–26.
17. Loth E, Faeth GM. Structure of underexpanded round air jets submerged in water. *Int J Multiph Flow* 1989;**15**(4):589–603.
18. Loth E, Faeth GM. Structure of plane underexpanded air jets into water. *AlChE J* 1990;**36**(6):818–26.
19. Dai ZQ, Wang BY, Qi LX, et al. Experimental study on hydrodynamic behaviors of high-speed gas jets in still water. *Acta Mechanica Sinica* 2006;**22**(5):443–8.
20. Shi HH, Wang BY, Dai ZQ. Research on the mechanics of underwater supersonic gas jets. *Sci China Phys Mech Astron* 2010;**53**(3):527–35.
21. Shi HH, Guo Q, Wang C, et al. Oscillation flow induced by underwater supersonic gas jets. *Shock Waves* 2010;**20**(4):347–52.
22. Weiland C, Vlachos PP. Round gas jets submerged in water. *Int J Multiph Flow* 2013;**48**:46–57.
23. He MS, Qin LZ, Liu Y. Oscillation flow induced by underwater supersonic gas jets from a rectangular Laval nozzle. *Procedia Eng* 2015;**99**:1531–42.
24. Huang N, Chen ZH, Wang ZL. Main characteristics of underwater supersonic gas jet flows. *Math Probl Eng* 2022;**2022**:1191938.
25. Zhang XY, Li SP, Yang BY, et al. Flow structures of over-expanded supersonic gaseous jets for deep-water propulsion. *Ocean Eng* 2020;**213**:107611.
26. Zhang XY, Li SP, Yu D, et al. The evolution of interfaces for underwater supersonic gas jets. *Water* 2020;**12**(2):488.
27. Tang JN, Wang NF, Shyy W. Flow structures of gaseous jets injected into water for underwater propulsion. *Acta Mechanica Sinica* 2011;**27**(4):461–72.

28. Zhang XY, Li SP, Yang BY, et al. Analysis of the flow instability of supersonic gaseous jets for submarine vehicles working in deep water. *Acta Armamentarii* 2019;**40**(12):2385–98 [Chinese].
29. Fronzeo MA, Kinzel M. An investigation of gas jets submerged in water. *46th AIAA fluid dynamics conference*. Reston: AIAA; 2016.
30. Tang YL, Li SP, Liu Z, et al. Horizontal jet characteristics of an underwater solid rocket motor at the beginning of working. *Acta Phys Sin* 2015;**64**(23):234702.
31. Tang YL, Li SP. The mechanism for the quasi-back-attack phenomenon of gas jets submerged in water. *Int J Aeronaut Space Sci* 2019;**20**(1):165–71.
32. Gong ZX, Lu CJ, Li J, et al. The gas jet behavior in submerged Laval nozzle flow. *J Hydrodyn* 2017;**29**(6):1035–43.
33. Liu J, Cong S, Song Y, et al. Flow structure and acoustics of underwater imperfectly expanded supersonic gas jets. *Shock Waves* 2022;**32**(3):283–94.
34. Jana A, Hoskoti L, Sucheendran MM. A numerical study of the flow field driven by a submerged, high-speed, gaseous jet. *J Fluids Eng* 2022;**144**(11):111208.
35. Tang LS, Liu Y, Wu ZF, et al. Experimental study on characteristics of bubble growth and pressure wave propagation by supersonic gas jets under water. *J Propuls Technol* 2011;**32**(3):417–20 [Chinese].
36. Zhang C, Yu W, Wang BS. Research on the initial flow field characteristics of underwater supersonic gas jets. *Acta Armamentarii* 2018;**39**(5):961–8 [Chinese].
37. Moon H, Han S, You Y, et al. Hybrid rocket underwater propulsion: A preliminary assessment. *Aerospace* 2019;**6**(3):28.
38. Liu W, Li N, Weng CS, et al. Bubble dynamics and pressure field characteristics of underwater detonation gas jet generated by a detonation tube. *Phys Fluids* 2021;**33**(2):023302.
39. Liu W, Li N, Huang XL, et al. Experimental study of underwater pulse detonation gas jets: Bubble velocity field and time-frequency characteristics of pressure field. *Phys Fluids* 2021;**33**(8):083324.
40. Zhang XW, Yu YG, Zhou LL. Numerical study on the multiphase flow characteristics of gas curtain launch for underwater Gun. *Int J Heat Mass Transf* 2019;**134**:250–61.
41. Xue XC, Yu YG, Zhang Q. Study on the effect of distance between the two nozzle holes on interaction of high pressure combustion-gas jets with liquid. *Energy Convers Manag* 2014;**85**:675–86.
42. Zhao JJ, Yu YG. The interaction between multiple high pressure combustion gas jets and water in a water-filled vessel. *Appl Ocean Res* 2016;**61**:175–82.
43. Xue XC, Yu YG, Zhao JJ. Study on draining off water mechanism and interaction characteristic of high-temperature and high-pressure combustion-gas jets with the water. *Appl Therm Eng* 2018;**143**:570–81.
44. Ma YJ, Bao FT, Hui WH, et al. A model for igniter mass flow rate history evaluation for solid rocket motors. *Int J Aerosp Eng* 2019;**2019**:2593602.
45. Guan D, Li SP, Sui X, et al. Mechanism of influence of high-speed self-spin on ignition transients for a solid rocket motor: a numerical simulation. *Propellants Explo Pyrotec* 2020;**45**(7):1040–56.
46. Chawla TC. The Kelvin-Helmholtz instability of the gas-liquid interface of a sonic gas jet submerged in a liquid. *J Fluid Mech* 1975;**67**(3):513–37.
47. Zhou YZ, Cai Z, Li QL, et al. Review of atomization mechanism and spray characteristics of a liquid jet in supersonic crossflow. *Chin J Aeronaut* 2023;**36**(8):1–23.
48. Zhang YW, Wang XH. Influence of outline of missile tail on the thrust of solid motor launching under water. *J Aerospace Power* 2008;**23**(5):927–31 [Chinese].
49. Chu RX, Xue MY, Wang Y, et al. Numerical simulation of underwater supersonic jet of vehicle with shell-shaped flow control structure. *J Appl Fluid Mech* 2023;**16**(11):2290–9.
50. Östlund J, Damgaard T, Frey M. Side-load phenomena in highly overexpanded rocket nozzles. *J Propuls Power* 2004;**20**(4):695–704.
51. Verma SB, Stark R, Haidn O. Relation between shock unsteadiness and the origin of side-loads inside a thrust optimized parabolic rocket nozzle. *Aerosp Sci Technol* 2006;**10**(6):474–83.